DEUTSCHES ELEKTRONEN-SYNCHROTRON **DESY**

DESY 87-165
RAL 87-113
December 1987

DEVELOPMENT OF THE ZEUS DETECTOR

by

ZEUS Collaboration

ISSN 0418-9833

NOTKESTRASSE 85 · 2 HAMBURG 52

To be sure that your preprints are promptly included in the
HIGH ENERGY PHYSICS INDEX ,
send them to the following address (if possible by air mail) :

DESY
Bibliothek
Notkestrasse 85
2 Hamburg 52
Germany

DESY 87-165
RAL 87-113
December 1987
ISSN 0418-9833

DEVELOPMENT OF THE ZEUS DETECTOR

ZEUS Collaboration

Presented at the DESY Theory Workshop
12-14 October 1987

by

D H Saxon
Rutherford Appleton Laboratory
Chilton, Didcot, Oxon, OX11 0QX

ZEUS - Carlton, Manitoba, McGill, Toronto, York (Canada), Bonn, DESY, Freiburg, Hamburg - I, Hamburg - II, Jülich, Siegen (Germany), Weizmann (Israel), Bologna, Cosenza, Firenze, Frascati, L'Aquila, Lecce, Milano, Padova, Palermo, ENEA-Roma, Roma, Trieste, Torino (Italy), Tokyo-INS, Tokyo-Metropolitan (Japan), NIKHEF-Amsterdam (Netherlands), Krakow, Warszawa (Poland), Madrid (Spain), Bristol, London - IC, London - UC, Oxford, Rutherford (UK), Argonne, Columbia, Illinois, Ohio State, Pennsylvania State, Virginia Polytechnic Institute and State University, Wisconsin (USA).

A B S T R A C T

ZEUS is a detector for $e^{\pm}p$ collisions at HERA. It is designed with the best possible hadronic energy resolution in mind. A depleted-uranium calorimeter provides a resolution of $0.35\,E^{-\frac{1}{2}} \oplus .02$ and hermetic coverage. Charged particles are tracked to resolution $\sigma_p/p = 0.002p \oplus 0.003$ (90°) and < 0.01p for angles above 140 mrad. A vertex detector measures impact parameters to 50 μm accuracy. Forward and barrel muon systems measure and identify muons with a hadron rejection of 10^{-3}. Silicon calorimeter pads and transition radiation detectors provide excellent electron identification. The luminosity monitor also tags photons at $Q^2 = 0$, and leading protons are detected over a wide momentum range.

ΖΕΥΣ - Ζήτησις καθ' Εὕρετης Ὑποκειμένης Συμμετρίας
ZEUS - Search to Elucidate Underlying Symmetry.

1. OVERVIEW

Lepton-hadron scattering has provided a key to unlock the structure of the proton, and of the weak currents coupling to quarks and leptons [1]. Just as the work of Hofstadter et al showed the component nucleons inside the helium nucleus [2], so scattering at 4.9-16 GeV at SLAC and DESY pinpointed the hard parton structure inside the nucleon [3,4], now identified as due to spin-½ quarks with fractional charges and the expected weak couplings [5,6]. A crucial experiment at SLAC in 1978 scattered electrons of fixed helicity off deuterons. The change in the cross-section on reversing the electron helicity showed a clear parity-violating effect, and the first evidence for the existence of a Z° boson which couples to charged particles [7]. Our present understanding of nature rests in large part on this foundation.

HERA provides polarised $e^{\pm}$ beams and a massively increased energy range. For 30 GeV electrons and 820 GeV protons the cm energy is 314 GeV and events will be seen with $Q^2 > 30000$ GeV^2. At the opposite extreme the x range down to 0.001 will be available to measure gluon distributions and look for quark substructure. Figures 1 and 2 illustrate the range of phenomena to be studied. Figure 1(a) shows the momentum vectors of the recoil lepton and the jet at different values of Q^2 and x. In order to exploit the unique window of HERA on high-Q^2 charged-current events we need excellent jet-energy resolution and calibration [8]. Otherwise the smearing corrections are too great for useful measurements to be made [9]. Figure 1(b) shows the gain in the (Q^2, x) plane when improving the fractional hadron energy resolution from $0.60/\sqrt{E}$ to $0.35/\sqrt{E}$ (E in GeV). The Q^2-range is extended and one obtains a factor 1.7 more well measured events. By contrast Figure 2 shows a simulated $ep \rightarrow t\bar{t}X$ event. In this case there is a profusion of low energy particles at wide angles to the beam.

To study the wide range of anticipated phenomena, we have developed the ZEUS detector (Figure 3). It has the following characteristics:

Calorimeter. This is hermetic ($2.2° < \theta < 176.5°$, covering 99.8% of the forward hemisphere and 99.5% of the rear) and has the best possible hadron energy resolution.

A depleted-uranium/scintillator calorimeter is used (DUCAL), with depth varying between 7 λ (forward direction) and 4 λ (rear). Such a calorimeter, with 499 tons of depleted uranium, absorbs 95% of the energy of 95% of the jets incident on it [10,11]. This provides hadron energy resolution $\sigma(E)/E = 0.35\ E^{-\frac{1}{2}} \oplus 0.02$. The DUCAL is surrounded by a backing calorimeter (BCAL - 7.5 cm Fe plates/Aℓ proportional tubes: $\sigma(E)/E = 1.0\ E^{-\frac{1}{2}}$). which improves the energy resolution by measuring the tails of showers, and also identifies "precision events" which are contained fully in the high-resolution detector. The calorimeter design implies that for electrons $\sigma(E)/E = 0.17\ E^{-\frac{1}{2}} \oplus 0.01$.

Tracking. A central magnetic field of 1.8 T provides accurate measurement of charged tracks through the central, forward and rear tracking detectors (CTD, FTD, RTD). $\sigma(p)/p = 0.002\ p \oplus 0.003$ at 90°, $\sigma(p)/p < 0.01\ p$ ($\theta > 140$ mrad), $\sigma(\theta,\phi) \lesssim 0.001$. With a vertex detector close to the beam pipe the impact parameter resolution is about 50 μm.

Lepton identification. For electrons in jets pion rejection of 10^{-4} is obtained in the forward cone over a wide momentum range (see Figure 4). This uses energy-momentum balance (tracking/calorimeter), for a layer of transition radiation detector (TRD), and silicon pad detectors (3 x 3 cm²) at the peak of the electromagnetic shower in the calorimeter. dE/dx from tracking (< 6% resolution) helps at low energies. In the barrel region hadron rejection better than the expected prompt lepton fraction is expected up to 25 GeV/c.

For muon identification we use double track-momentum measurement (inner detector + toroids) and tracking through the BCAL. In the forward direction, where lepton momenta are high, a system of several magnetised toroids is used. We expect $\sigma(p)/p \sim 20\%$ for p = 100 GeV/c in the forward direction and 30% for p = 20 GeV/c in the barrel. Pion rejection factors of 1000 (p = 40 GeV/c, forward) and 500 (p = 10 GeV/c, barrel) are obtained.

Forward particles. A leading proton detector measures protons leaving down the beam pipe with 1% resolution and high acceptance over a wide momentum range ($0.3 < x_L < 1$). On the other side zero-degree photon and forward electron detectors provide a luminosity monitor (via $ep \rightarrow ep\gamma$), as well as tagging exchanged photons and providing an optional veto for hard initial-state bremsstrahlung events, in order to remove the most rapidly varying part of radiative corrections.

The readout environment is dominated by the 96 ns inter-crossing interval, less than, for example, the 500 ns maximum of drift time in the CTD. This leads us to the development of pipelined data acquisition and trigger. The ZEUS work is therefore in the forefront of developments needed for future colliders, such as LHC and SSC, with 15-25 ns crossing intervals [12,13].

The ZEUS detector is described fully elsewhere [11,14]. Here we outline the approach that has been followed in developing the detector design.

2. THE CALORIMETERS

The energy of a particle or jet of charged and neutral particles is measured efficiently in a calorimeter with a fractional resolution that improves as $E^{-\frac{1}{2}}$ (because of the increase in shower statistics) and a detector depth that grows only as log E. To obtain sufficient hadronic absorption lengths in a reasonable space one uses dense (and therefore high Z) absorber plates interspersed with active detector layers, usually of lower Z (see Figure 5(a)). For an electromagnetic shower in such a sampling calorimeter one expects:

$$\frac{\sigma(E)}{E} = 0.05 \sqrt{\frac{\Delta E(1 + 1/N_{pe})}{E}}$$

for an electron of E GeV, losing ΔE MeV/layer with N_{pe} electrons seen per minimum ionising particle (mip) per layer [15]. For 3 mm DU (depleted uranium) 2.5 mm scintillator and $N_{pe} = 4$, $\sigma/E = 0.14\ E^{-\frac{1}{2}}$.

In a detector with high Z absorber/low Z detector, electrons leave a signal less than that of a minimum ionising particle (say a muon) [16]. This is because the energy lost by the electrons is detected downstream,

and migrates to regions of high Z, as can be seen from the Z-dependence of the energy-detecting processes: ionisation and Compton scattering (Z^1), pair production and bremsstrahlung (Z^2) and, the dominant contribution, photoelectric effect (Z^5). Thus e/mip is about 0.6 for DU/Sci, 0.7 for Pb/liquid argon, 0.85 for Fe/Sci, 0.95 for Cu/liquid argon.

For hadrons the situation is more complicated and the losses are greater. A hadronic shower has, compared to an electromagnetic shower, fewer interactions (each of high multiplicity) and a large unknown loss of energy (the binding energy of the struck nucleon) at each interaction. A variable fraction is lost in neutrinos, and each time a π^0 is made, the energy is deposited much more locally (on a scale X_0(rad) $\sim$ 1 cm, not λ(int) $\sim$ 15 cm) as an electromagnetic shower. The result is that there is significantly less energy deposited (typically 70% of that from an electron-initiated shower of the same energy), but a widely varying distribution, reaching all the way up to the electron energy for those occasional cases where the shower is dominated by π^0s (see Figure 6(a)). Such calorimeters typically yield, after corrections to spot local clusters of energy due to π^0s, a resolution of (0.5 to 0.6) $E^{-\frac{1}{2}}$[18,19].

In a depleted uranium-scintillator calorimeter, neutron spallation and γ-emission provide an opportunity to compensate for the hadronic energy loss [21,15,16,20]. If one adjusts the calorimeter properties to achieve exact compensation, e/h = 1, then hadron energy resolutions of (0.30 to 0.35) $E^{-\frac{1}{2}}$ are achieved [21]. The following effects determine the response of a DU-scintillator to hadronic showers:

- Ionisation by charged particles (dE/dx).
- Electromagnetic showers from the decay of π^0, giving e/mip $\sim$ 0.6. The low energy component ($E \leq 1$ MeV) is mostly lost into the DU by photoelectric effect.
- Hadron-nucleus collisions. One loses typically 15-20% of the energy to nuclear binding and neutrinos [21], but gains fissions (4.1/GeV for 300 GeV pions) and spallation neutrons (450 neutrons of $\sim$ 3 MeV for 10 GeV protons) over a timescale of order 100 ns (somewhat matched to the HERA inter-crossing time).
- Spallation neutrons give np elastic scatters on the free hydrogen in the scintillator. (For a detector such as liquid argon without free hydrogen this mechanism is negligible, although γ-emission gives some compensation.)
- The slow protons ionise the scintillator. $\beta \sim 0.08$ and $dE/dx \sim 1/\beta^2$ so saturation effects are important. The light output follows Birks' law

$$\frac{dL}{dx} = \frac{S\ dE/dx}{1 + K_B\ dE/dx}$$

($K_B \sim 0.01$ g cm^{-2} MeV^{-1} - see Figure 7.)

One sees that electrons give a signal 40% below a mip. Hadrons are suppressed even further, but the compensation mechanism, through np scatters in a hydrogenous detector (such as scintillator or tri-methyl-pentane), provides an enhancement. By adjusting the detector

parameters, one can achieve compensation within 1-2%. The energy resolution will be [22]:

$$\frac{\sigma(E)}{E} = \frac{0.22}{\sqrt{E}} \oplus 0.09 \sqrt{\frac{\Delta E(1 + 1/N_{pe})}{E}}$$

for 3 mm DU, 2.5 mm Scintillator, $N_{pe} = 4$, $\sigma/E = 0.33\ E^{-1/2}$.

Figure 8 shows a test setup used to study the resolution of a DU-scintillator calorimeter and Figure 6(b) some results. Compensation and improved resolution are seen when DU is used. Since spallation occurs in all heavy elements, compensation can be achieved with Pb/Sci. A resolution of $0.45\ E^{-1/2}$ has been achieved, the best seen in a non-uranium calorimeter, but with an electromagnetic resolution degraded to $0.24\ E^{-1/2}$ [24].

Figure 9 compares our predictions of compensation (e/h) as a function of plate thickness, with the results of tests [14,16]. As a result of this theoretical and experimental experience, one is able to pick a precise configuration and predict its performance [25]. Figure 10 shows results up to 100 GeV beam energy. Linearity is better than ± ½%. For hadrons in the energy range 10-100 GeV we find:

$$\sigma/E = 0.34\ E^{-1/2} \oplus 0.013$$

From this experience we proceed to the design of the high resolution calorimeter, shown in Figure 11. Each calorimeter tower consists of repeated units of depleted uranium and scintillator, as shown in Table 1. Each DU plate is clad in steel to reduce the radioactivity emitted to a level that does not provide a troublesome background to energy measurement, but does provide a ready, universal, absolute stability monitor. Each calorimeter tower has 146 to 186 such layers. The towers are 20 x 20 cm with three depth segmentations (EMC, HAC1, HAC2 except at the rear) readout with wavelength shifter bars both sides to photomultipliers at the rear (see Figure 12). The front (EMC) section has 5 x 20 cm towers. In the barrel region (BEMC, BHAC) the towers have a wedge shaped layout (32 sectors), and a pointing EMC section. In all there are 7612 electromagnetic readout channels and 5228 hadronic channels. There are 499 tons of depleted uranium, and 23 tons of scintillator.

A calorimeter of great statistical precision has an advantage only if its systematic errors (calibration, uniformity, time dependence) can be controlled equally well. Figure 13 illustrates some aspects of this showing almost no change in attenuation length (a) with radiation dose (b) with time, and great uniformity by the use of reflection masks (c) across the scintillator of an EMC tower and (d) in depth down a wavelength shifter bar. The irregularities across cracks are also found to be very small [25]. No cracks point at the vertex.

Electrons are identified in the calorimeter by matching the measured energy to the momentum measured in the tracking chambers. A large improvement (x 100) is made if the pulse height is sampled close to the shower maximum. This is done using 3 x 3 cm^2 Si pads (a size matched to the EM shower diameter) to catch electrons in showers. Figure 14 shows the pulse height distributions after 5.4 X_0 for hadron and electron beams. In the silicon system alone, hadron rejections of 100 are achieved at 90%

T A B L E 1

COMPOSITION OF A LAYER DU + SCI IN HADRON CALORIMETER

Material	Thickness (mm)	X_0	λ
Steel	0.4	0.023	0.0024
DU	3.3	1.000	0.0305
Steel	0.4	0.023	0.0024
Sci	2.6	0.006	0.0033
Paper	0.7		
Contingency	0.6		
Sum	**8.0**	**1.052**	**0.0386**

Effective X_0	0.76 cm
Effective λ	20.7 cm
Effective R_M	2.0 cm
Effective Critical Energy	12.3 MeV
Effective Density	8.7 g/cm³

electron efficiency at 50 GeV, and the use of two sampling layers (at 3.6 and 7.2 X_0) achieves the same rejection down to 3 GeV.

The hadron energy measurement is completed by the backing calorimeter. This detector (Figure 15) has extruded aluminium proportional tubes between 7.5 cm thick layers of iron. It provides measurement of the energy in the tail of a shower to resolution 1.0 $E^{-1/2}$, or can be used to define events contained fully in the uranium. Triangular cathode paths provide measurement of a through-going muon trajectory to 2 mm accuracy along the wire.

3. MUON IDENTIFICATION

Lepton identification is a key element of QCD studies and of searches for new phenomena at HERA. In contrast to LEP, where the virtual photon or Z° treats all generations equally, HERA has a first-generation initial state. Any difference in behaviour for outgoing electrons and muons is a signature for new physics within a generation, for example right-handed or excited leptons [26]. It is therefore essential to have excellent muon detection over as large a solid angle as possible, as well as the electron identification provided by the calorimeters and the tracking detectors.

The muon detector is necessarily large (see Figure 3) with over 3000 m² of limited streamer tubes. It has to perform the following functions:

- Identify a muon by a minimum-ionising track penetrating through the calorimeter.

- Measure the sign of the charge of the track over the full momentum range, including the forward direction where the momenta are highest. For this reason the backing calorimeter is magnetised toroidally and muon trajectories measured on entry and exit. Additional toroids strengthen the forward detector.

- Identify the muon as coming from the primary interaction or a short lived (< 10^{-12} s) decay. This demands continuous tracking through the inner detector, measurement of impact parameter, and a comparison of inner and outer detector momentum measurements.

- Provide a trigger for rare muon events as a signal for new physics.

A prompt muon is tracked with up to 80 consecutive measurements through the inner tracking chambers, including the vertex detector (to guard against decay in flight), extrapolated through the depleted uranium, and measured through the backing calorimeter. The iron of the backing calorimeter is magnetised toroidally (B = 1.6 T), and the trajectory is measured in muon chambers at four planes (two co-ordinates each plane), to provide position and direction information both inside and outside the iron. We thus obtain a very strong muon signature, by remeasuring both trajectory and momentum.

The layout of the barrel muon detectors is shown in Figure 3(b), together with the coils used to magnetise the iron. The barrel muon detector is constructed using double-layers of limited streamer tubes (LSTs) of non-flammable construction, with two co-ordinates read out (see Figure 16(a)). A honeycomb structure holds two double layers rigidly over an octant of the detector (Figure 16(b)). Relative alignments are monitored continuously at the octant boundaries to an accuracy of 15 μm. The tube size (9 mm) is chosen to limit the drift time to 96 ns, so that there is no crossing-number ambiguity (Figure 16(c)). Position accuracies of 150 μm are achieved, giving a momentum error of 30% at 30 GeV/c. (Most of the error is due to multiple scattering in the iron.)

Higher momentum muons are anticipated in the forward direction. A stronger analysis system is therefore constructed with two additional iron toroids, and five planes of LSTs (r, ϕ co-ordinates) and time of flight to give a trigger and four planes of drift chamber (r co-ordinate) measuring momentum (see Figure 3(a)). Additional LST walls complete the angular coverage between the forward toroids and the barrel region. Figure 17(a) shows the momentum resolution for different regions of polar angle and 17(b) the trigger efficiency as a function of momentum.

Both the barrel and the forward muon detector systems provide event triggers, by looking for coincidences between inner and outer layers separated by iron, and demanding candidate tracks through them. This provides triggers for exotic and heavy flavour physics, as well as for cosmic ray tests.

4. THE INNER TRACKING DETECTORS

The tasks and environment of the tracking detectors dictate the form of the detector chosen (Figure 18) [27]. We wish to reconstruct tracks in jets - an excellent two track resolution (2.5 mm) is needed, and many points on a track for unambiguous track following (9 x 8 superlayers radially, 9 x 6 in the forward direction). We need to reconstruct exotic events - and so need an unambiguous sign measurement for $p_T \leq 150$ GeV/c, ie $\sigma_p/p < 0.003\ p$ (GeV/c): we chose a high magnetic field (1.8 T). We need strong lepton identification - vertex accuracy, momentum and charge accuracy for both e and μ, dE/dx and TRD for e, and continuity of tracking as a protection against decay in flight for μ. Vertex accuracy is needed in addition for heavy flavours and exotics, and we need a vertex trigger

as a protection against the dominant background of off-trajectory protons that otherwise confuse the charged-current trigger. The detector has to be continuously live to new events but have a powerful rejection of out-of-time crossings (96 ns interval).

A segment of the central tracking detector is illustrated in Figure 19(a). It is constructed as a stereo superlayer chamber, or 'vector drift chamber', with nine superlayers (alternately axial and small angle stereo) each with eight layers. Each superlayer is capable of reconstructing a track vector, and chains of track vectors are subsequently linked together (see Figure 19(b)). The philosophy is similar to that of the CDF, Mark II and SLD detectors [13, 28-31]. Table 2 gives some characteristics of the chamber together with performance figures measured in recent tests [32].

The high repetition rate of HERA forces a short maximum drift path (2.5 cm = 500 ns) and demands a strong out-of-time rejection technique. The short maximum drift time also allows the tracking chambers to contribute to the level-1 trigger. To achieve this, we take advantage of the high magnetic field, and the resulting large rotation of electron drift away from the electric field lines. We design for a 'Lorentz angle' of 45°, by balancing the electric field and alcohol concentration against the magnetic field [30]. Sophisticated design calculations optimise the uniformity of drift, simultaneously with the uniformity of sense wire gain, and minimal electrostatic wire deflections [33,34]. Figure 20 illustrates electron drift trajectories and isochrones, and shows the dislocation and loss of points on a track, out of time by one crossing. One also sees in Figure 19(b) that left-right ambiguous solutions are readily rejected on grounds of lack of continuity, within and between superlayers.

Tracking is continued into the forward direction by the forward tracking detector. This is constructed in three modules. Each module has three superlayers at 60° relative orientations, and each superlayer has six sense layers (see Figure 21). More than 50 sense layers are crossed by all tracks at $\theta > 126$ mrad. The chambers are of low-mass construction, amounting to only 0.27 radiation lengths, and $0.39 \cdot X_0$ in the frames.

T A B L E 2

CENTRAL TRACKING DETECTOR PARAMETERS

4608 sense wires in 72 layers		
Gas $Ar/C_2H_6/C_2H_5OH$ 104 MHz FADC Readout	v_D = 50 μm/ns	
$\sigma(r\phi)$	100-200 μm	(θ-dependent)
$\sigma(z)$	1.0-1.4 mm	(stereo)
	3 cm - layers 1, 3, 5	(timing-trigger)
$\sigma(dE/dx)$	< 6%	(e^-)
Two track resolution	2.5 mm	
Magnetic field	1.8 T	
σ_p/p	0.0021 p ⊕ 0.0029 (90°)	
	0.0012 p ⊕ 0.0032 (45°)	

There is ± 150 μm stagger to resolve left-right ambiguity and a maximum drift length of 12 mm. In the event of high backgrounds due to bad running conditions, the central part of the chamber can be desensitised whilst operating the outer part normally. However, one expects only 0.2 γ/crossing to be absorbed in these chambers from collimator emissions in normal running.

A single rear tracking detector module (18 sense layers) is provided to improve the Q^2 resolution by measurements of the recoil electron direction at small (backward) angles. The FTD and RTD system has a total of 5796 sense wires.

Electron identification in the forward cone is strengthened by transition radiation detectors. There are four modules, two between FTD 1 and FTD 2, and two between FTD 2 and FTD 3. The radiator volume contains 20 μm diameter polypropylene fibres, and the emitted X-rays are absorbed in a $Xe-CO_2$ drift region. An amplification region (6 mm wire spacing) completes the 10 m deep module (Figure 22). Figure 23 illustrates the time structure of typical events from π and e beams. One sees contributions from dE/dx (π and e), and X-ray absorption (e) which is clustered in space (and therefore in time also). Electrons and hadrons are distinguished on the basis of total charge and number of clusters (estimated efficiently by looking at the total charge above threshold), making a maximum likelihood fit to the four modules. Test beam data indicate hadron rejection better than 10^{-2} at 90% electron efficiency. This performance is included in the hadron rejection levels shown in Figure 4 (see also Reference 35).

Two vertex detector concepts are currently under consideration - a time expansion chamber and an induction drift chamber. The time expansion chamber consists of two superlayers of staggered mini jet-cells, with up to 10 hits/track (see Figure 24). Precision is achieved by the use of unsaturated gas (dimethylether). The slow drift (∿ 6 μm/ns) provides the basis of the spatial precision, and two-track resolutions of 1.5 mm or better should be achieved (see also Reference 36). Limiting the maximum drift time to 500 ns gives a system of 230 cells with 832 sense wires. An elegant and compact construction, mounting the wires on alumina plates which themselves are the electronics boards, has been devised.

The vertex detector has to squeeze into the space between the beam pipe and the CTD. Figure 25(a) shows a possible induction chamber layout. The beam pipe is offset to allow for the one-side-dominated electron synchrotron radiation fan, whilst approaching as close as possible to the beam. Each shaded region is a double layer of low-mass construction. The principle of the induction chamber is illustrated in Figure 25(b). Anode wires are placed at 600 μm spacing. The position measurement is achieved by looking at the left-right asymmetry of the induced signals on the potential wires [37].

5. FORWARD-GOING PARTICLES

On the electron (downstream) side, we detect forward going electrons and photons using detectors as shown in Figure 26. The e-p splitter magnets act as an electron spectrometer, and Pb-scintillator-silicon electron calorimeter located at 30 m has high acceptance for $16 < E_e < 22$ GeV. Photons are detected at zero degrees by a γ-detector (carbon filter - $3X_0$, Cerenkov electron veto, Pb-scintillator-silicon) after 100 m.

The two detectors comprise a high-rate, luminosity monitor through the process $ep \rightarrow ep\gamma$. Systematic errors (estimated to be no more than 5%) are limited by knowledge of the beam properties, as this affects the calculated acceptance. In addition, these detectors extend the physics capabilities in two ways. First, the recoil electron tags the energy of virtual photons at $Q^2 = 0$ ($Q^2_{max} = 0.02$ GeV^2), between $8 < E_\gamma < 14$ GeV. Secondly, the forward γ-detector can be used to veto (or identify) initial state bremsstrahlung events. Efficient vetoing of these greatly eases the radiative correction calculations in, for example, the evaluation of the longitudinal structure function at very low-x [38].

The physics reach of the detector is extended in another direction by the leading proton detector. One approaches the downstream proton beam as close as possible with silicon strip detectors in Roman pots. The optics are complicated and the access difficult, and so to achieve a good acceptance one needs several (six) pots. The detector locations (S1-S6) and the acceptance as a function of the longitudinal proton momentum fraction (x_L) are shown in Figure 27. One reaches the diquark fragmentation region, as well as being enable to study, for example, the structure function of the Pomeron [39], or looking at high p_T jets in diffractive events [40].

Development and construction of the detector components described above is now underway. Working within a three-continent collaboration on such a large project is both an educational and a rewarding experience. Those of us from overseas owe a great deal to the support and enthusiasm of the DESY Laboratory.

REFERENCES

1. See for example D H Saxon, Proc Roy Soc Lond A404 (1986), 233.

2. R Hofstadter, Rev Mod Phys 28 (1956), 214.

3. W Bartel et al, Phys Lett 28B (1968), 148.

4. W K H Panofsky, Proc 14th Int Conf on High Energy Physics, Vienna 1968 (Ed J Prentki and J Steinberger), p 23.

5. E M Riordan et al, SLAC-PUB-1634 (1975).

6. F Dydak, Proc Int Symp on Lepton and Photon Interactions at High Energies, Cornell 1983 (Ed D Cassel and D L Kreinick), p 634.

7. C Prescott et al, Phys Lett 77B (1978), 347; 84B (1979) 524.

8. ZEUS - A Detector for HERA. Letter of Intent (June 1985).

9. E Longo, Proc Workshop on Experimentation at HERA, Amsterdam, 1983. DESY HERA 83/20, p 285.

10. M G Catanesi et al, Nucl Instr Meth A260 (1987) 43.

11. ZEUS Collaboration. The ZEUS Detector, Technical Proposal (March 1986).

12. J R Hansen, Proc Workshop on Physics at Future Accelerators (La Thuile and Geneva (1987)), CERN 87-07, Vol I p 274.

13. D H Saxon, Nucl Instr Meth (to be published).

14. ZEUS Collaboration. The ZEUS Detector, Status Report (September 1987).

15. G Wolf, DESY 86-089.

16. H Brückmann et al, DESY 86-155, DESY 87-064, NIM ???

17. H Abramowicz et al, Nucl Instr Meth 180 (1981), 429.

18. H1 Collaboration, W Braunschweig et al, DESY 87-098.

19. B Anders et al, DESY 86-105.

20. R Wigmans, CERN/EF 86-18.

21. C Fabjan and W Willis, Phys Rev Lett 60B (1975), 105.
C Fabjan et al, Nucl Instr Meth 141 (1977), 61.
T Akesson et al, Nucl Instr Meth A241 (1985), 17.

22. C W Fabjan and T Ludlam, Ann Rev Nucl Part Sci 32 (1982), 335.

23. R L Ford and W P Nelson, SLAC Report 210 (1978).

24. E Bernardi et al, DESY 87-041.

25. R Klanner, DESY 87-058.

26. R J Cashmore et al, Phys Rep 122 (1985) 275.

27. B Foster, Bristol preprint BRP/HEP 87-1, Proc X Warsaw Int Symp on High Energy Physics (Kazimierz, 1987) - to be published.

28. G Hanson et al, Nucl Instr Meth A252 (1986), 343.
A J Weinstein, UC Santa Cruz Report SCIPP 87/78.
J E Bartelt, SLAC-PUB-4084 (1986).

29. SLD Design Report, SLAC-Report-273 (1984) and updates.
W B Atwood et al, Nucl Instr Meth A252 (1986), 295.

30. F Bedeschi et al, "Design and Construction of the CDF Central Tracking Chamber".
M Atac et al, Nucl Instr Meth A249 (1986), 265.

31. D H Saxon, Proc Workshop on Physics at Future Accelerators (La Thuile and CERN), CERN 87-07, Vol I, p 205.

32. S M Tkaczyk et al, Rutherford Report RAL-87-094.
See also J A Blissett et al, Nucl Instr Meth 228B (1984), 45; A245 (1986), 291.

33. J H C Roberts, Rutherford Report RAL-87-095.

34. J P Berge (Private Communication).

35. M Holder and H Suhr, Siegen Report SI-87-15 (submitted to NIM).

36. A R Clark et al, LBL-23519 (submitted to NIM).

37. A H Walenta, Nucl Instr Meth 217 (1983), 65.
A H Walenta et al, Nucl Instr Meth (to be published).

38. A M Cooper-Sarkar et al (to be published).

39. A Donnachie and P V Landshoff, Nucl Phys B244 (1984), 322; B267 (1985), 690; Phys Lett 191B (1987), 309.

40. G Ingelman and P E Schlein, Phys Lett 152B (1985), 256.

FIGURE CAPTIONS

1. (a) Lepton and jet momentum vectors over the (Q^2, x) range for 30 GeV e on 820 GeV p. At high x and low Q^2 jets lie close to the beam. Also shown is the range explored by EMC. Running at intermediate energies will provide continuity.

   (b) Improvement in the range of well-measured CC events on changing the hadronic energy resolution from $0.60\ E^{-\frac{1}{2}}$ to $0.35\ E^{-\frac{1}{2}}$. The number of well-measured events also increases by a factor 1.7.

2. Topology of a simulated $\bar{t}t$ production event.

3. Vertical section through the ZEUS detector (a) along the beam (b) normal to the beam.

4. Hadron-electron rejection for electrons in jets in the FCAL: (a) energy and momentum balance within 2σ and transition radiation information (b) same + one-layer Si pad (c) the expected prompt e/h ratio in jets.

5. (a) Sketch of a sampling calorimeter

   (b) the e/mip ratio for several DU-scintillator structures, calculated with EGS [11].

6. Pulse height distributions for 5 GeV e, μ, h in (a) Pb-Sci (5 + 5 mm) (b) DU-Sci (3.2 + 5 mm) [15].

7. The ionisation loss and light output (arbitrary units) for protons with $K_B = 0.01$ g cm^{-2} MeV^{-1} [15].

8. Setup used for DU-scintillator tests [19].

9. Predictions for the e/h ratio for uranium scintillator and lead scintillator calorimeters. Measurements shown as crosses.

10. Calorimeter response to electrons, hadrons and muons at energies for 10 to 100 GeV.

11. The high resolution calorimeter layout.

12. Internal structure of a calorimeter tower, showing gaps for silicon detector. Note the breaks in the drawing in order to show detail at the start of HAC1 and HAC2.

13. Scintillator control of systematics: (a) attenuation after radiation does of 0 and 1.6 kGy (b) time dependence (in days) of attenuation length (c) uniformity across an EMC scintillator tower (d) uniformity along a wavelength shifter bar.

14. (a) Pulse height distributions for 5 GeV hadron and electron beams. Si pad detector after 5.4 X_0.

   (b) Hadron rejection as a function of electron efficiency.

   (c) Same with 2 planes at 3.6 and 7.2 X_0 depth.

15. Backing calorimeter (a) schematic of Aℓ proportional tubes (b) pulse height distribution for 50 GeV muons tracked through (c) same for 20 GeV electrons in test chamber with 5 cm iron plates.

16. (a) Cross-section of a barrel muon chamber.

    (b) Chamber support showing two double layers of LSTs, honeycombs and location of electronic cards at chamber ends.

    (c) Space-drift time relation within one LST cell. Lines - 50 μm/ns.

17. (a) Expected momentum resolution for forward muon detector as a function of momentum.

    (b) Trigger efficiency.

18. Layout of the inner tracking detectors: CTD - central tracking detector; FTD1, 2, 3 - forward tracking chambers; TRD - transition radiation detector; RTD - rear tracking detector; VXD - vertex detector.

19. (a) Layout of a CTD segment.

    (b) Simulated NC event, axial layers only, including left-right ambiguities.

20. Electron drift lines and isochrones (constant drift-time contours - 50 ns intervals). The points associated with a track, out of time by one crossing, are illustrated.

21. (a) Sketch of an FTD chamber with three superlayers of different wire orientation.

    (b) Cross-section of drift cells.

    (c) Number of sense layers traversed as a function of polar angle.

22. Cross-section through one 10 cm deep TRD module. Sense wires are spaced 6 mm apart.

23. Time structure of typical events in a TRD module.

24. (a) Equipotentials and (b) Drift lines in a TEC cell.

25. (a) Arrangement of the chamber modules for the IDC vertex detector.

    (b) Principle of the induction chamber.

26. The forward electron spectrometer (35 m long) and the forward photon detector (105 m).

27. (a) The layout of the forward proton detector.

    (b) Acceptance as a function of $x_L = p_L$ (proton)/p(beam).

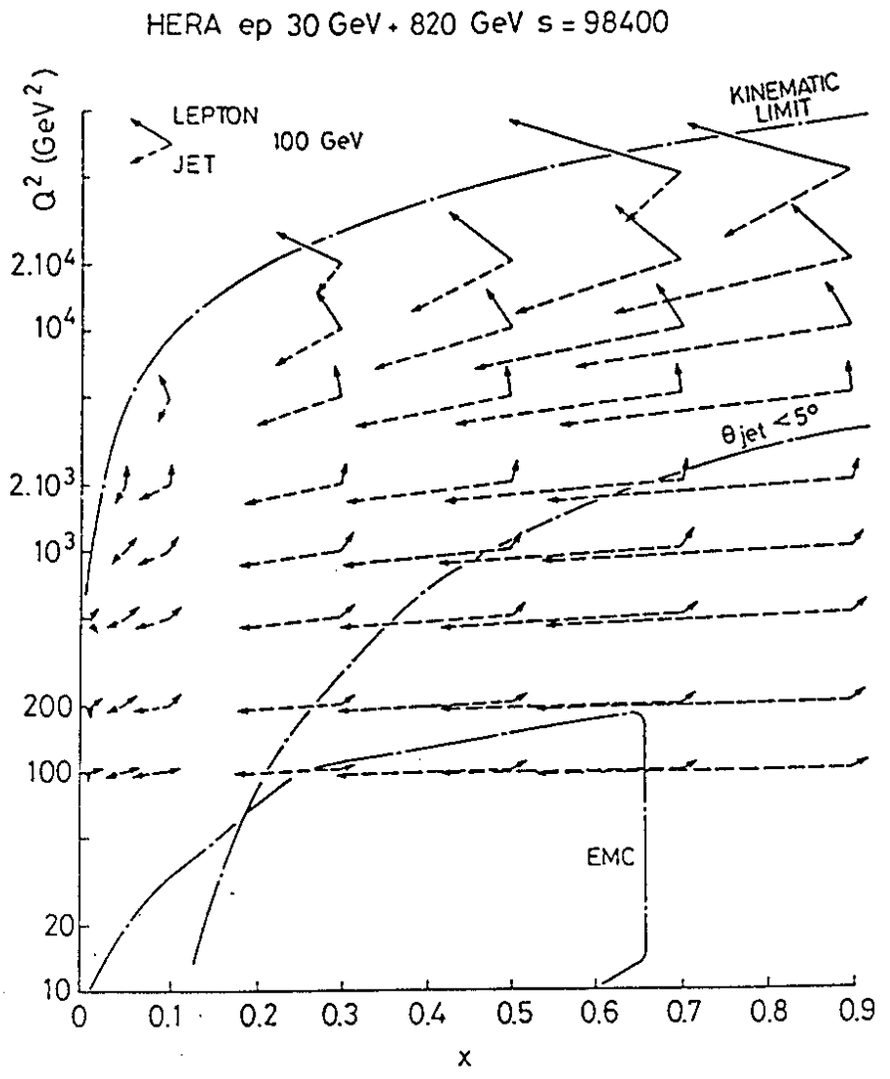

FIG 1(a)

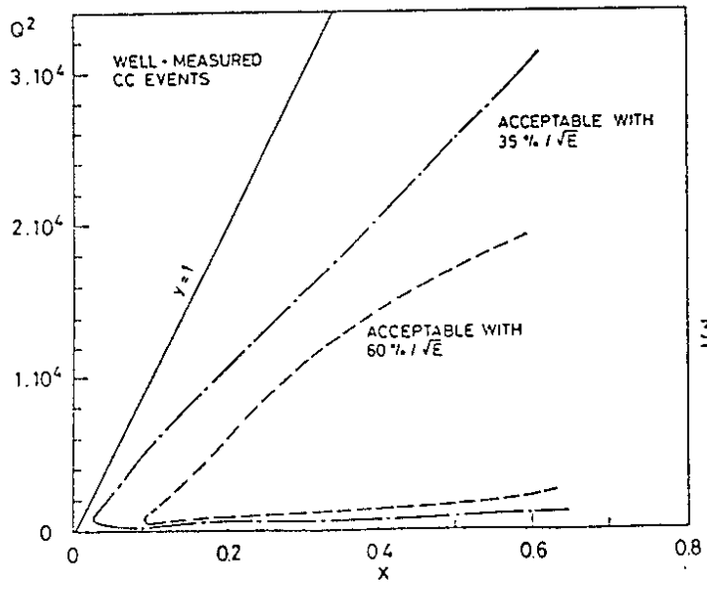

FIG 1(b)

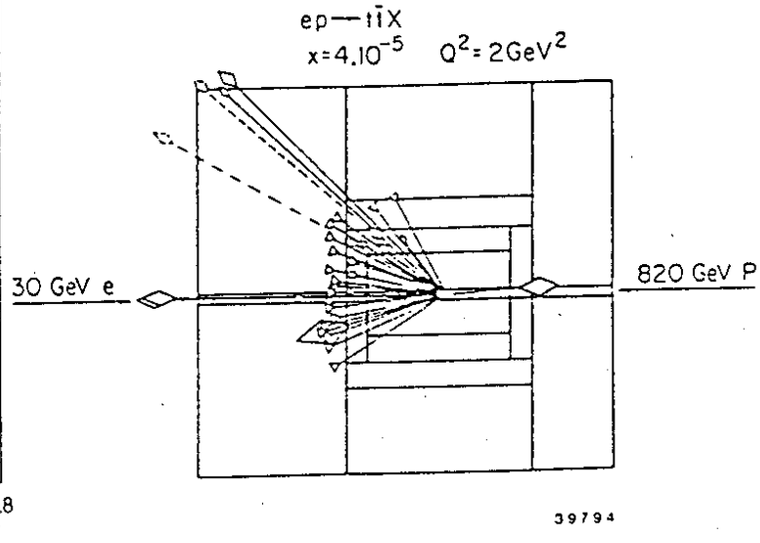

FIG 2

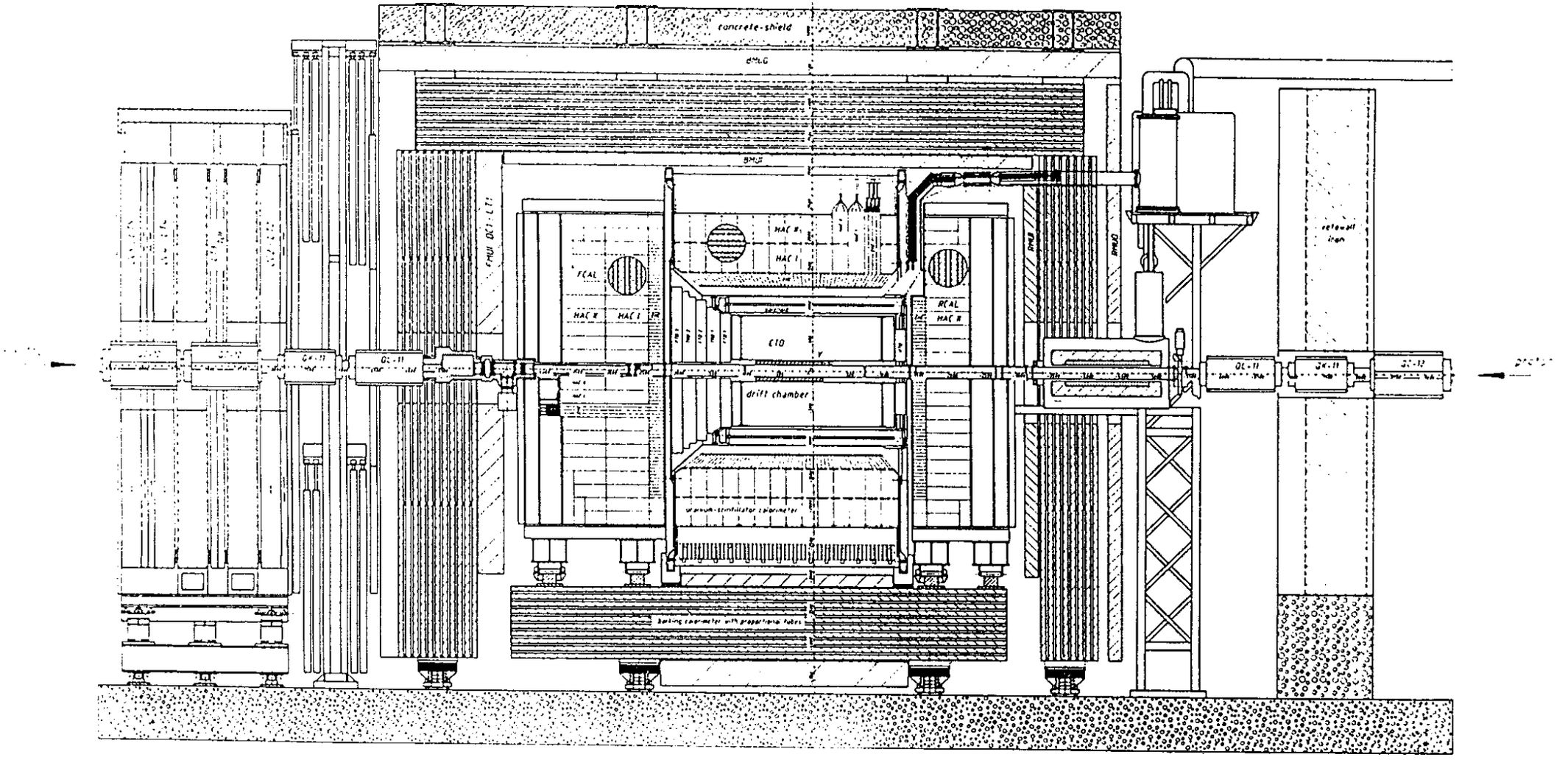

FIG 3(a) Section of the ZEUS detector along the beam.

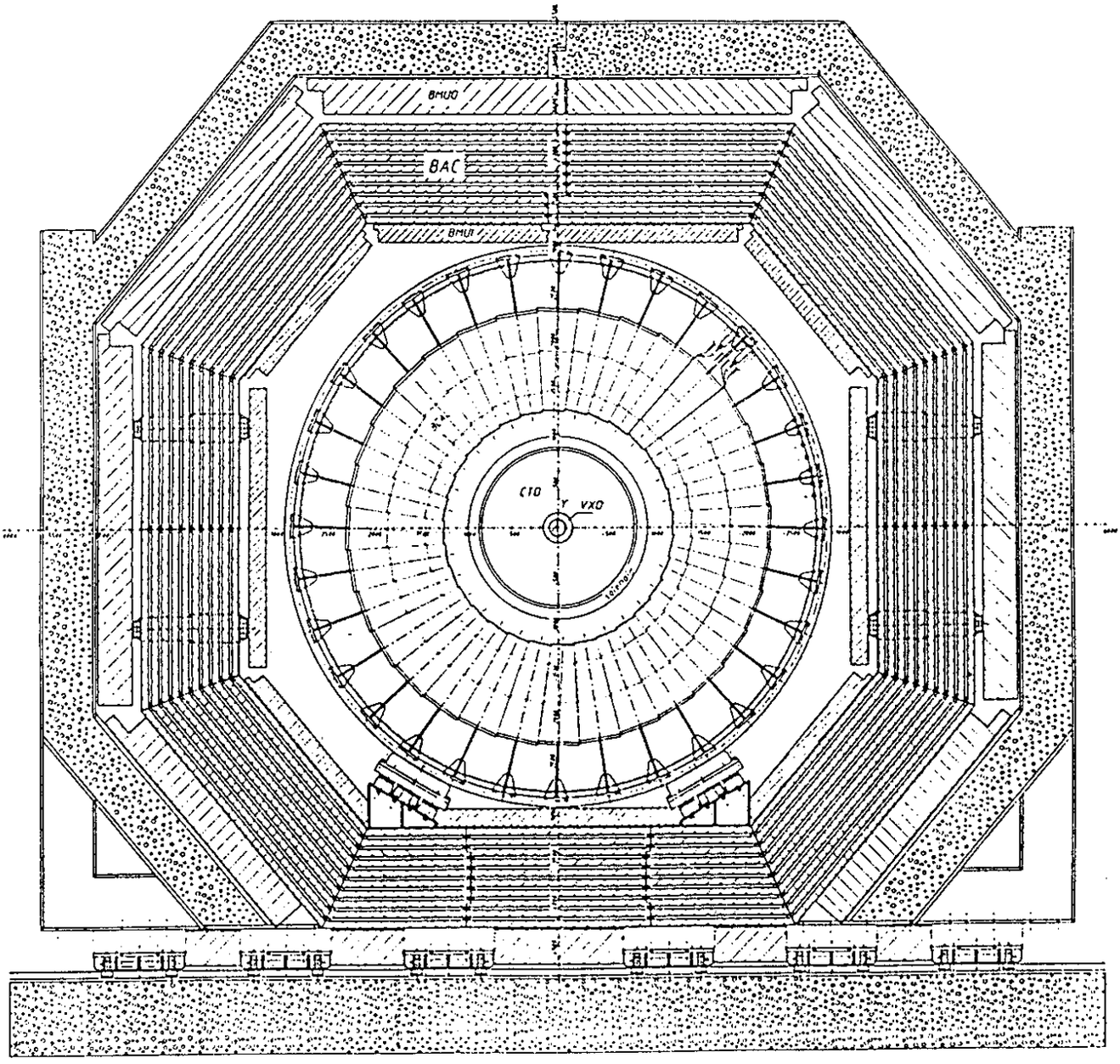

FIG 3(b) Section of the ZEUS detector perpendicular to the beam.

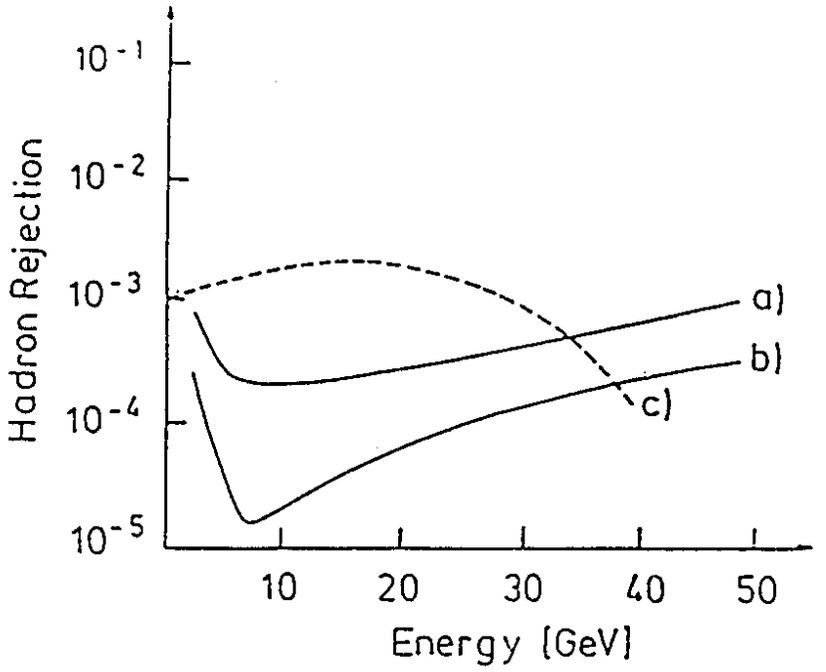
Hadron Rejection
10⁻¹
10⁻²
10⁻³
10⁻⁴
10⁻⁵
a)
b)
c)
10
20
30
40
50
Energy [GeV]

FIG 4

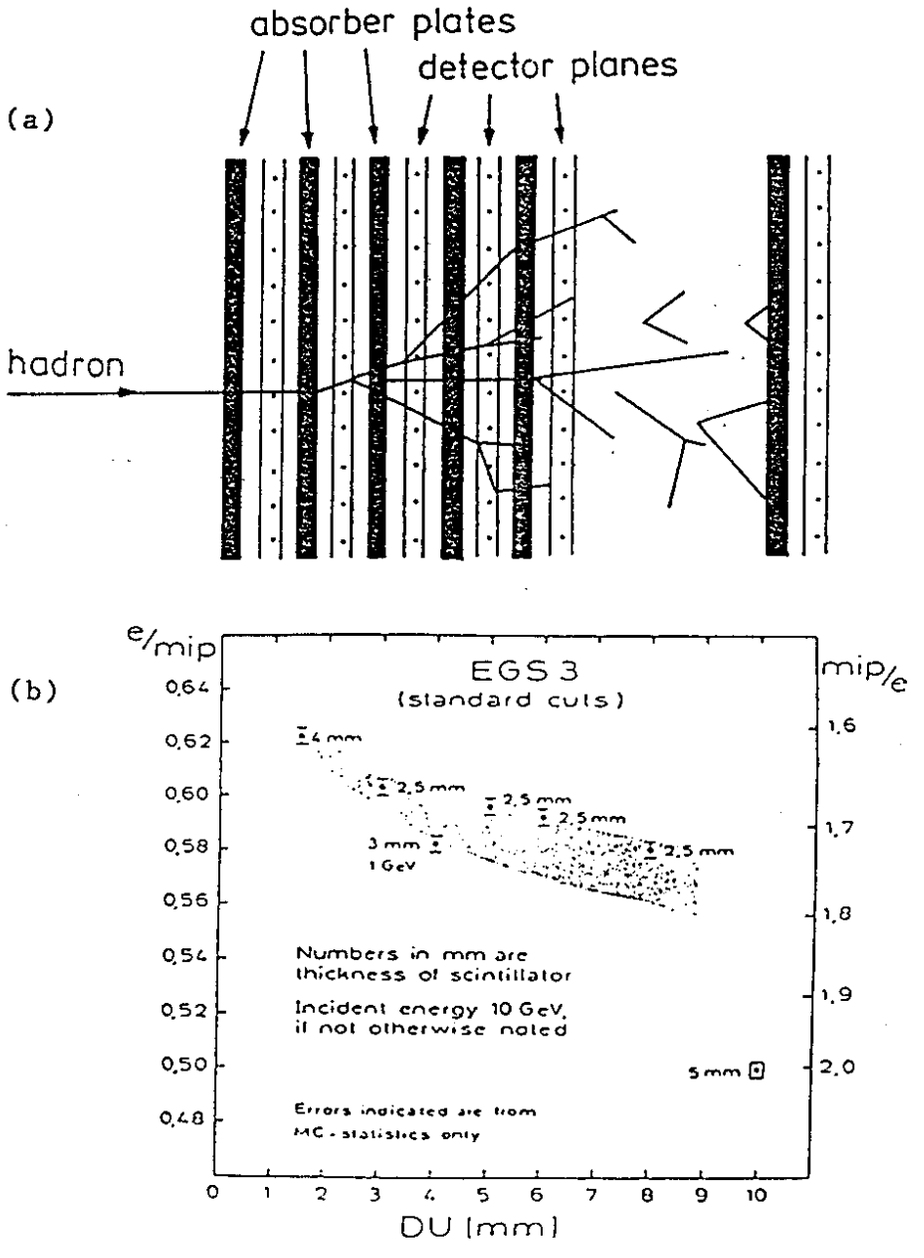
(a)
absorber plates
detector planes
hadron
(b)
e/mip
mip/e
EGS 3
(standard cuts)
4 mm
2.5 mm
2.5 mm
2.5 mm
2.5 mm
3 mm
1 GeV
Numbers in mm are
thickness of scintillator
Incident energy 10 GeV,
if not otherwise noted
5 mm
Errors indicated are from
MC - statistics only
0,64
0,62
0,60
0,58
0,56
0,54
0,52
0,50
0,48
1,6
1,7
1,8
1,9
2,0
0 1 2 3 4 5 6 7 8 9 10
DU [mm]

FIG 5

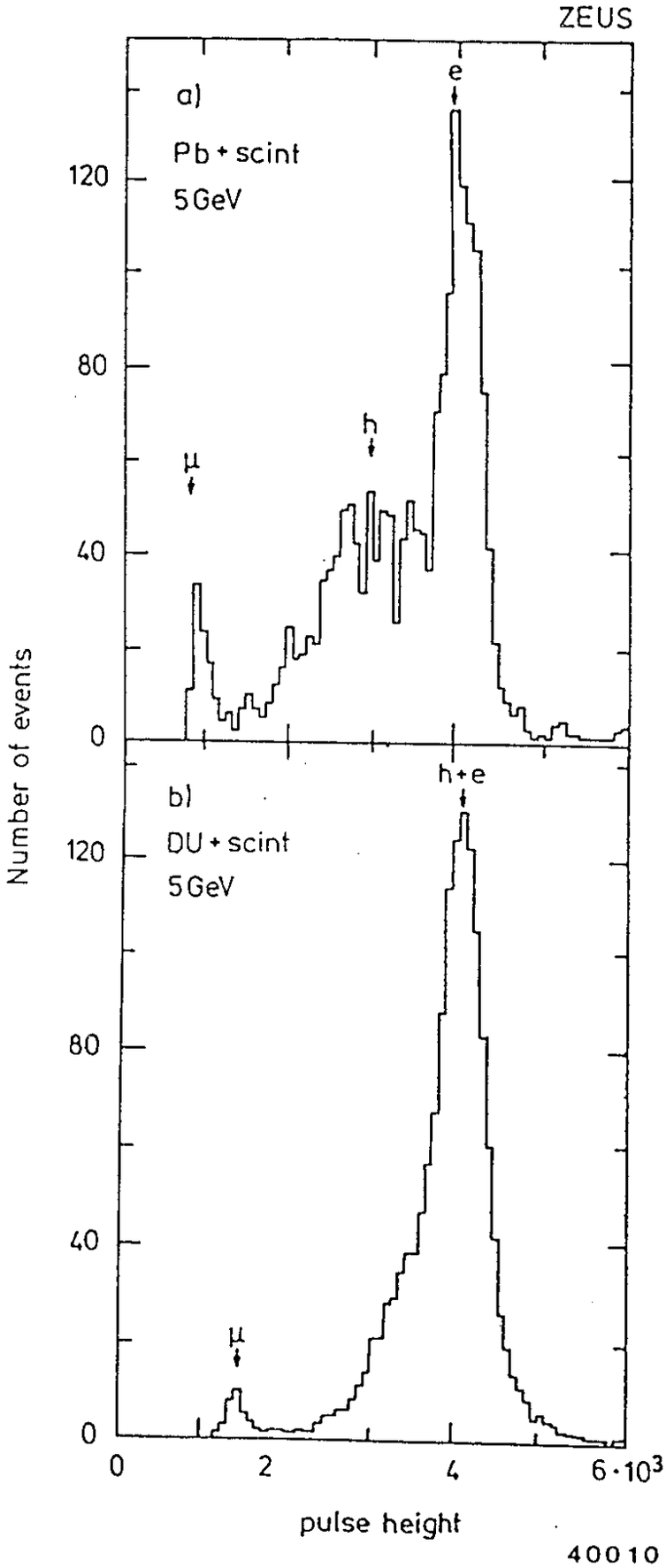
ZEUS
a)
Pb + scint
5 GeV
e
h
μ
120
80
40
0
b)
DU + scint
5 GeV
h+e
μ
120
80
40
0
0
2
4
6·10³
Number of events
pulse height
40010

FIG 6

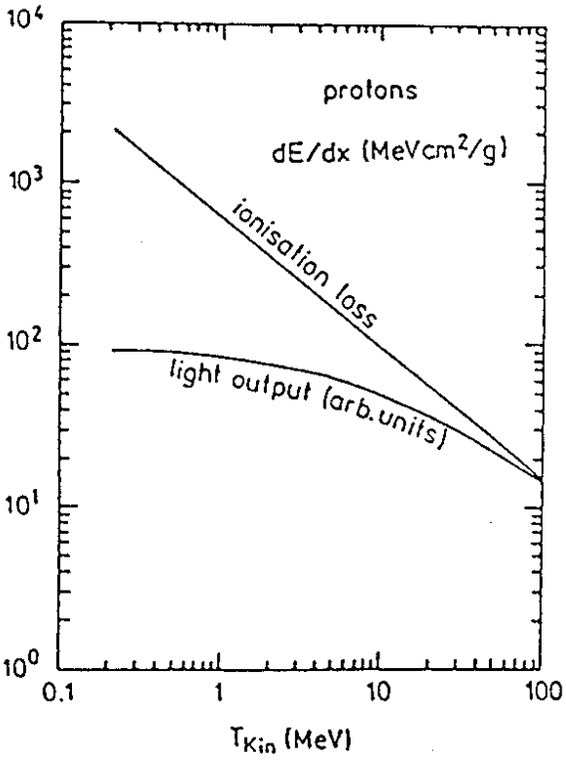
protons
dE/dx (MeVcm²/g)
ionisation loss
light output (arb. units)
10⁴
10³
10²
10¹
10⁰
0.1
1
10
100
T_Kin (MeV)

FIG 7

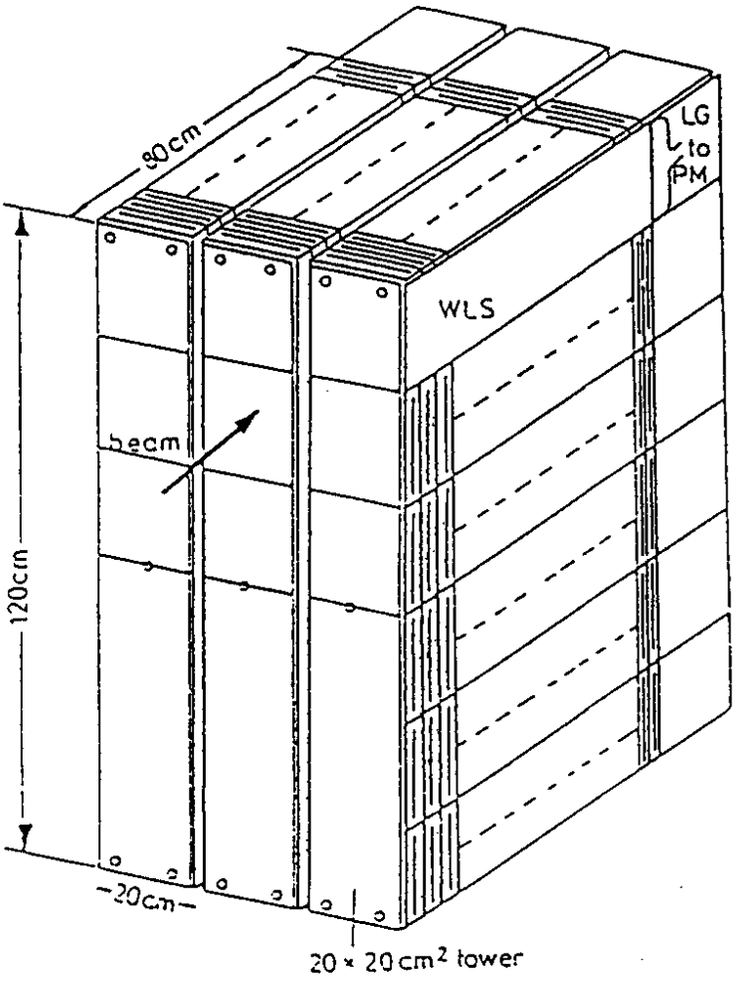
80cm
LG
to
PM
WLS
beam
120cm
20cm
20 × 20 cm² tower

FIG 8

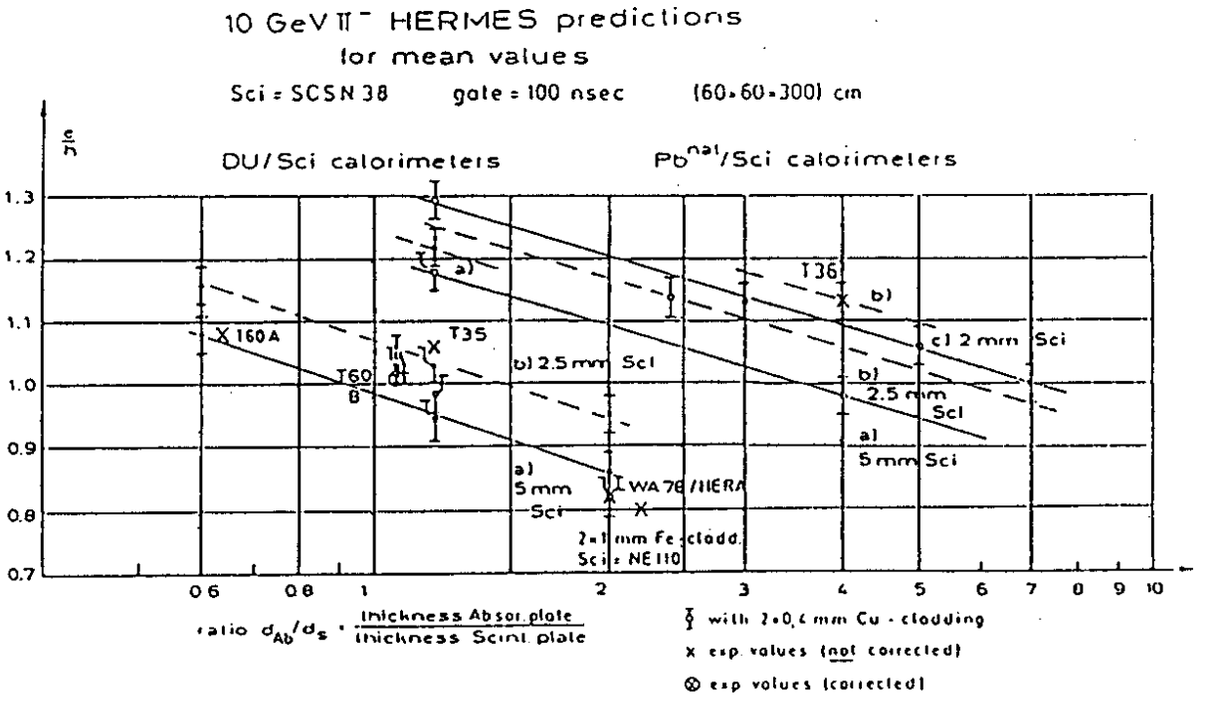
10 GeV π⁻ HERMES predictions
for mean values
Sci = SCSN 38 gate = 100 nsec (60×60×300) cm
DU/Sci calorimeters
Pb^nat/Sci calorimeters
T60
T35
T36
160A
a)
b) 2.5 mm Sci
b)
2.5 mm
Sci
c) 2 mm Sci
a)
5 mm Sci
a)
5 mm
Sci
WA 78 /HERA
2×1 mm Fe-cladd.
Sci: NE 110
1.3
1.2
1.1
1.0
0.9
0.8
0.7
0.6
0.8
1
2
3
4
5
6
7
8
9
10
ratio d_Ab/d_s = thickness Absor. plate / thickness Scint. plate
with 2×0.4 mm Cu - cladding
x exp. values (not corrected)
⊗ exp. values (corrected)

FIG 9

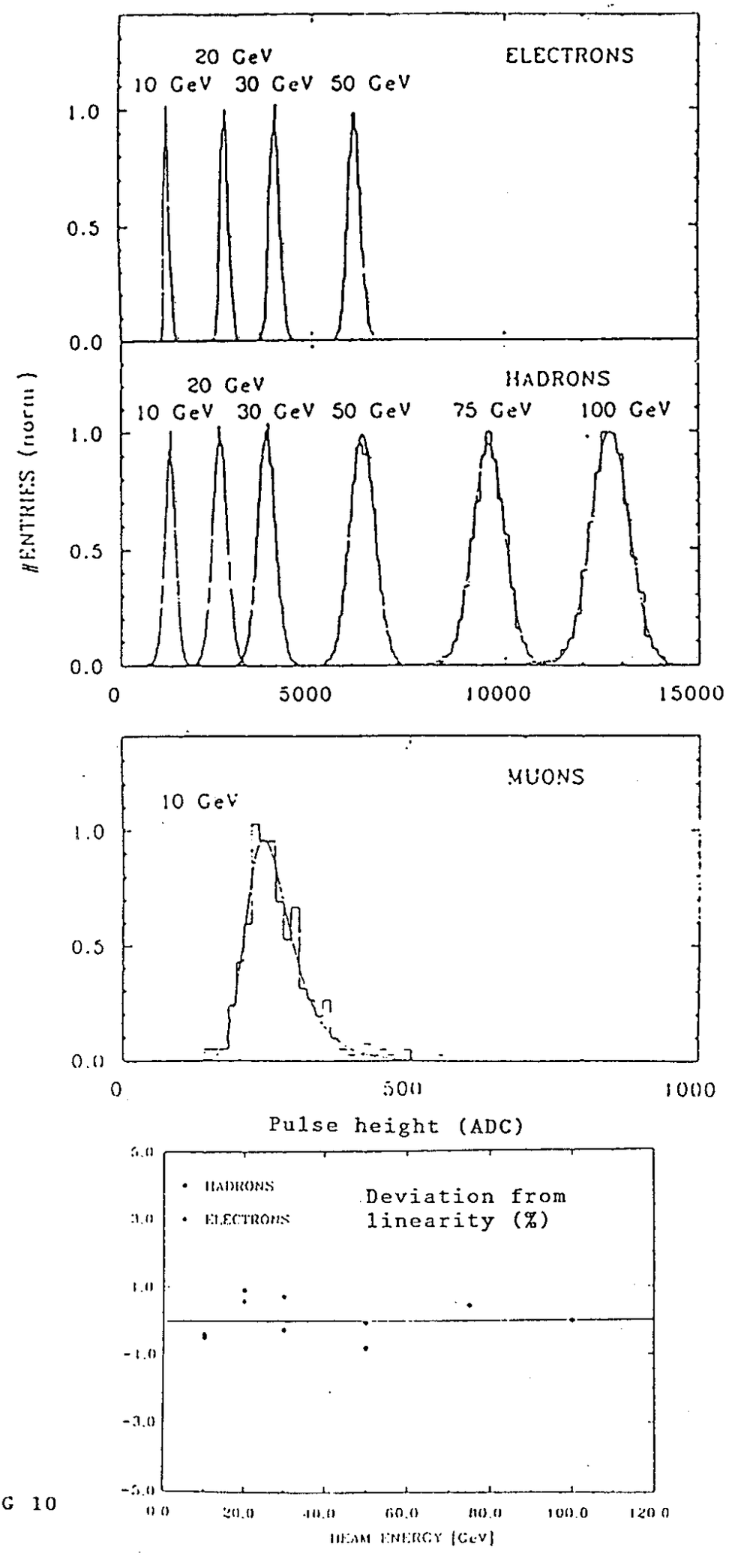
20 GeV
10 GeV 30 GeV 50 GeV
ELECTRONS
1.0
0.5
0.0
20 GeV
10 GeV 30 GeV 50 GeV 75 GeV 100 GeV
HADRONS
#ENTRIES (norm.)
0
5000
10000
15000
MUONS
10 GeV
500
1000
Pulse height (ADC)
HADRONS
ELECTRONS
Deviation from linearity (%)
BEAM ENERGY (GeV)

FIG 10

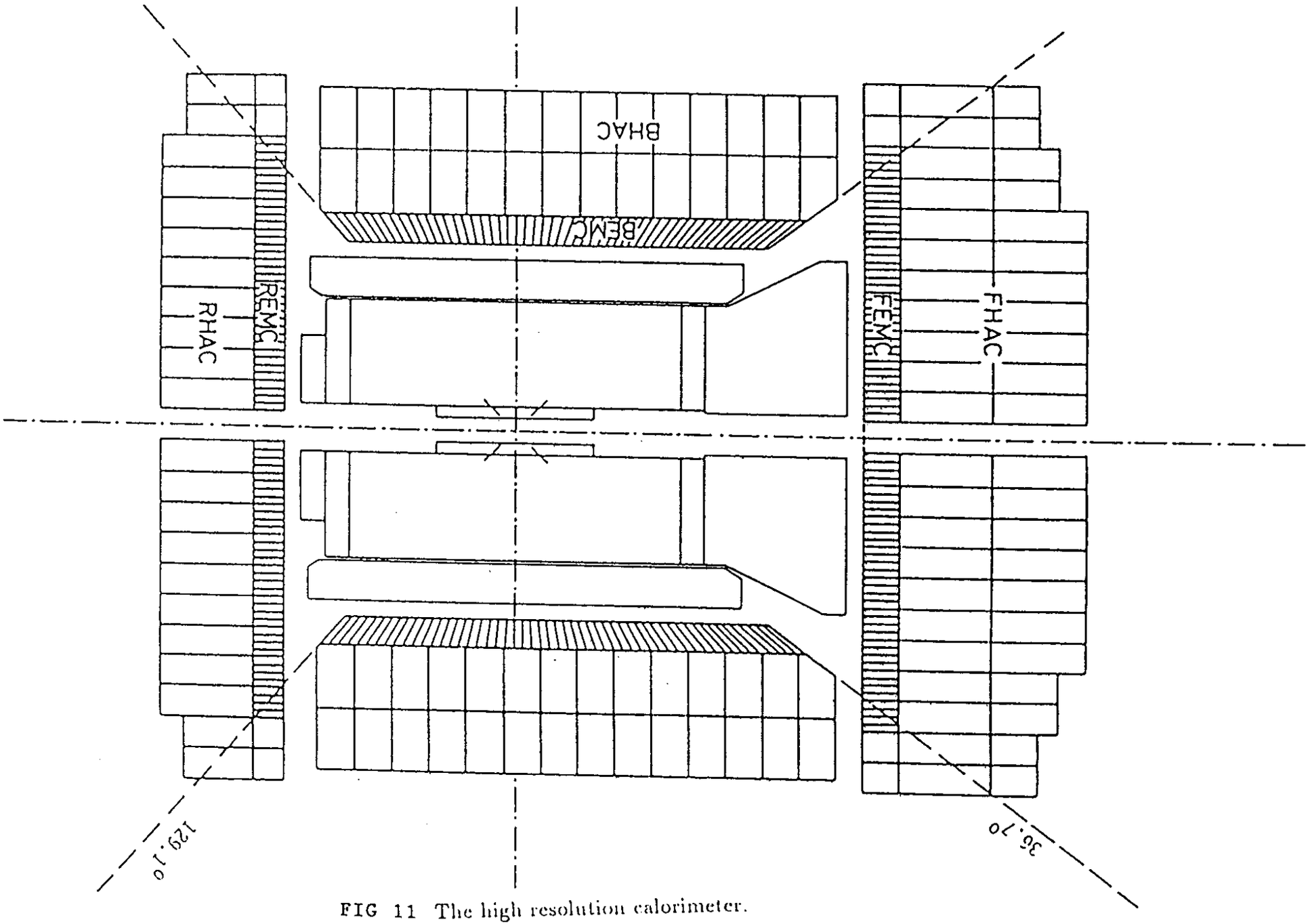

FIG 11 The high resolution calorimeter.

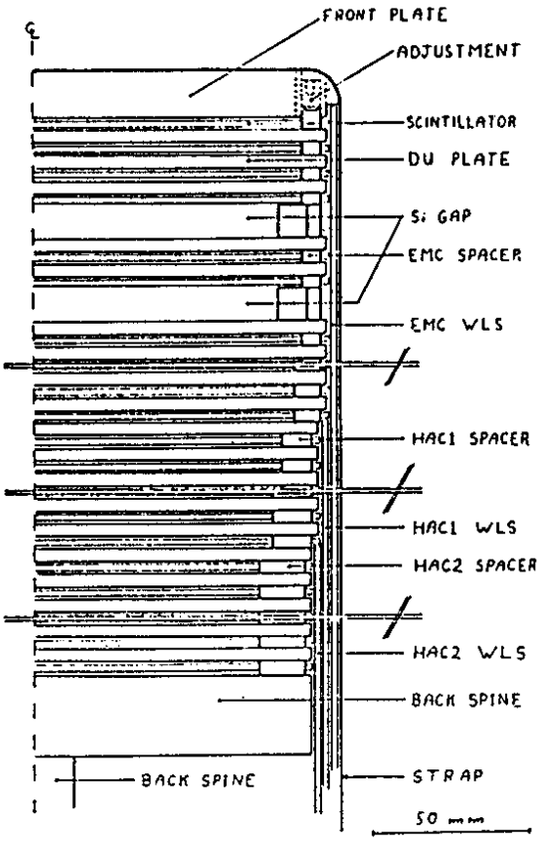

FIG 12

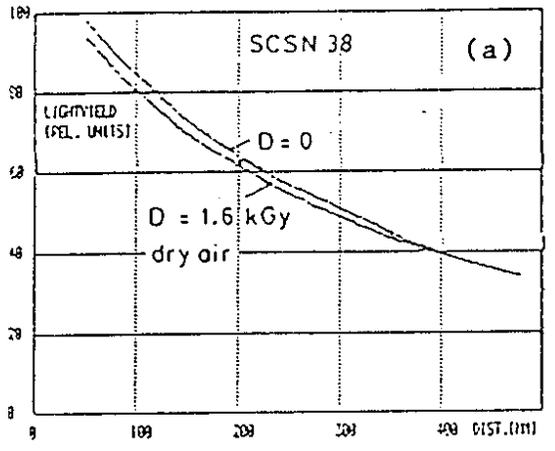

(b)

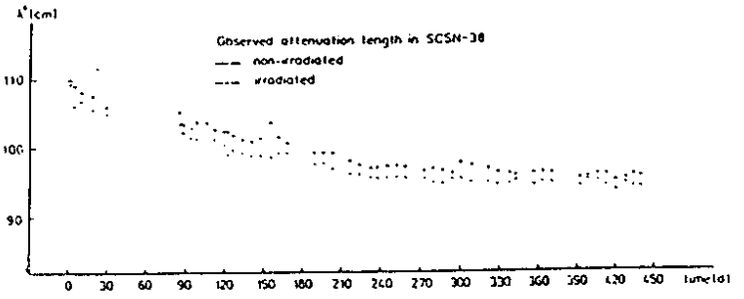

(c)

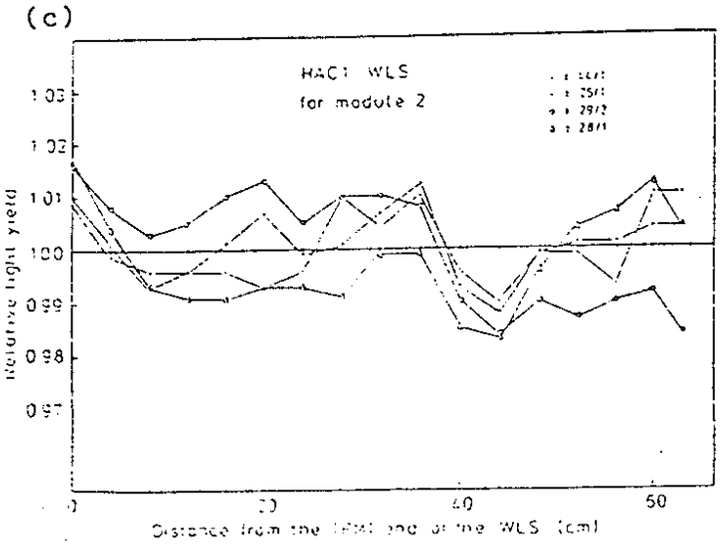

(d)

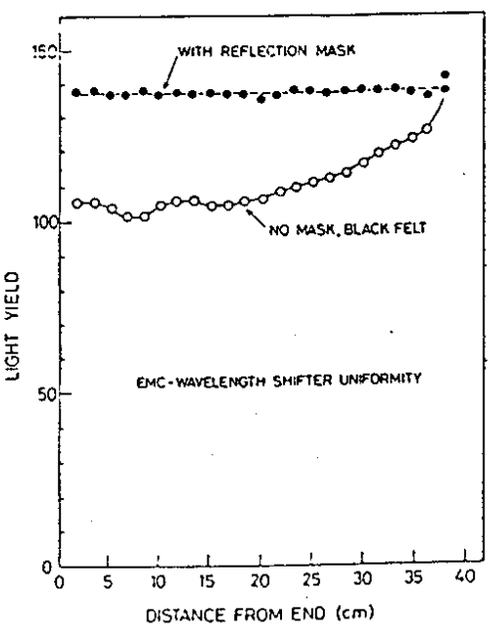

FIG 13

(a)

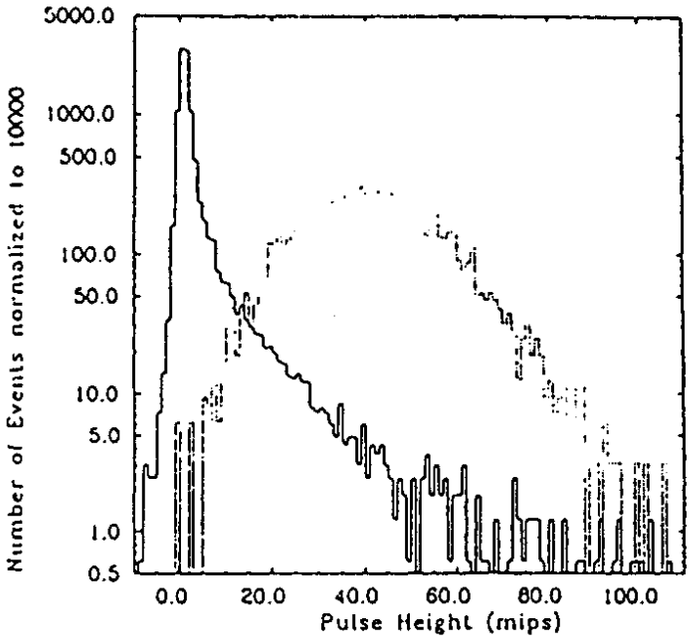
5000.0
1000.0
500.0
100.0
50.0
10.0
5.0
1.0
0.5
Number of Events normalized to 10000
0.0
20.0
40.0
60.0
80.0
100.0
Pulse Height (mips)

(b)

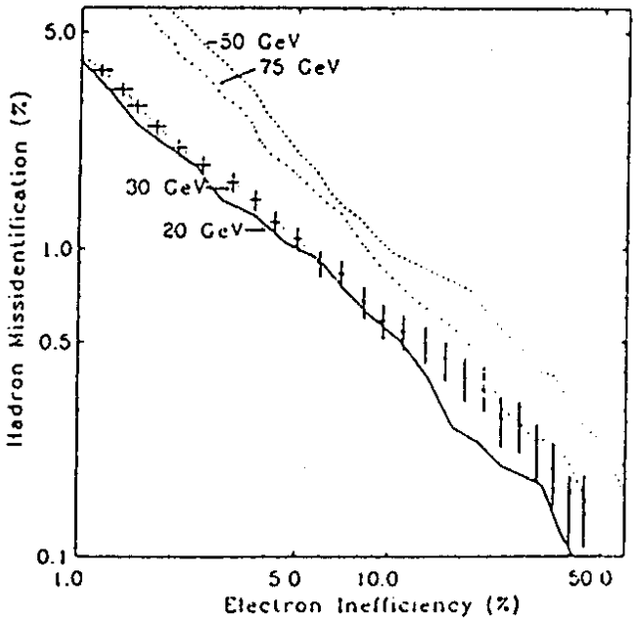
5.0
1.0
0.5
0.1
Hadron Missidentification (%)
50 GeV
75 GeV
30 GeV
20 GeV
1.0
5.0
10.0
50.0
Electron Inefficiency (%)

(c)

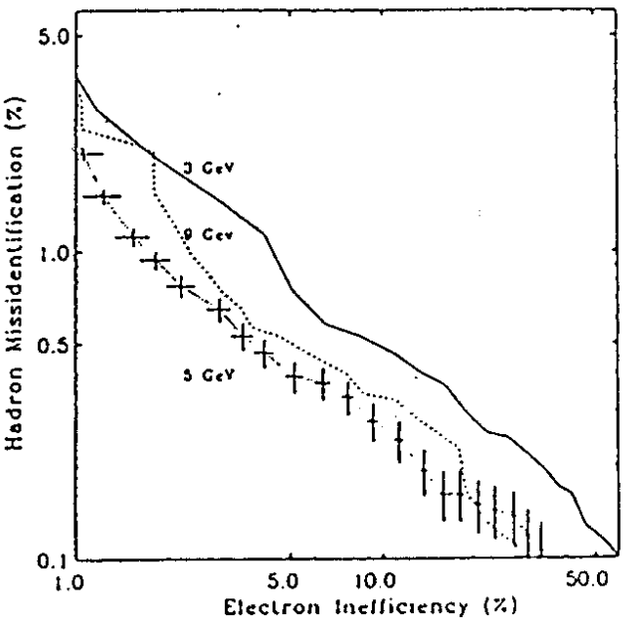
5.0
1.0
0.5
0.1
Hadron Missidentification (%)
3 GeV
9 GeV
5 GeV
1.0
5.0
10.0
50.0
Electron Inefficiency (%)

FIG 14

(a)

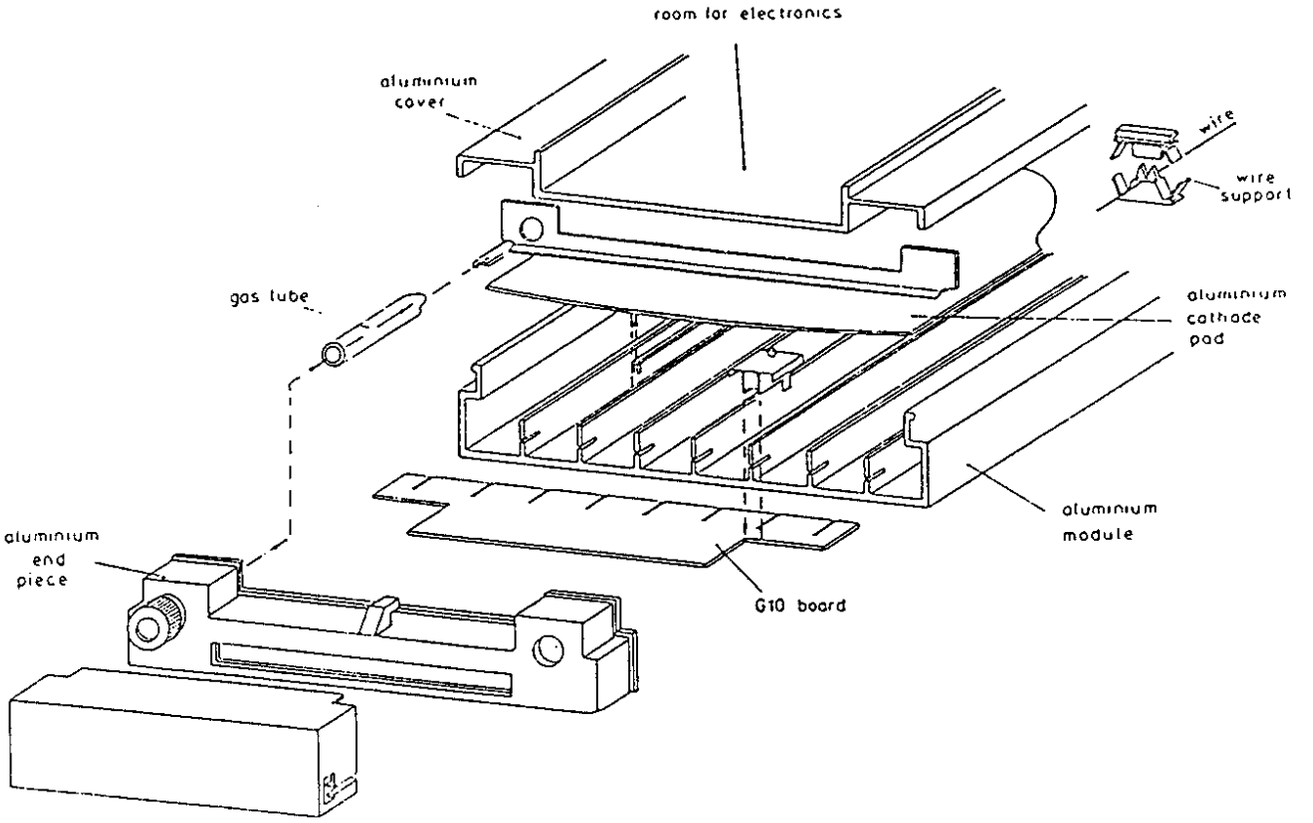

(b) (c)

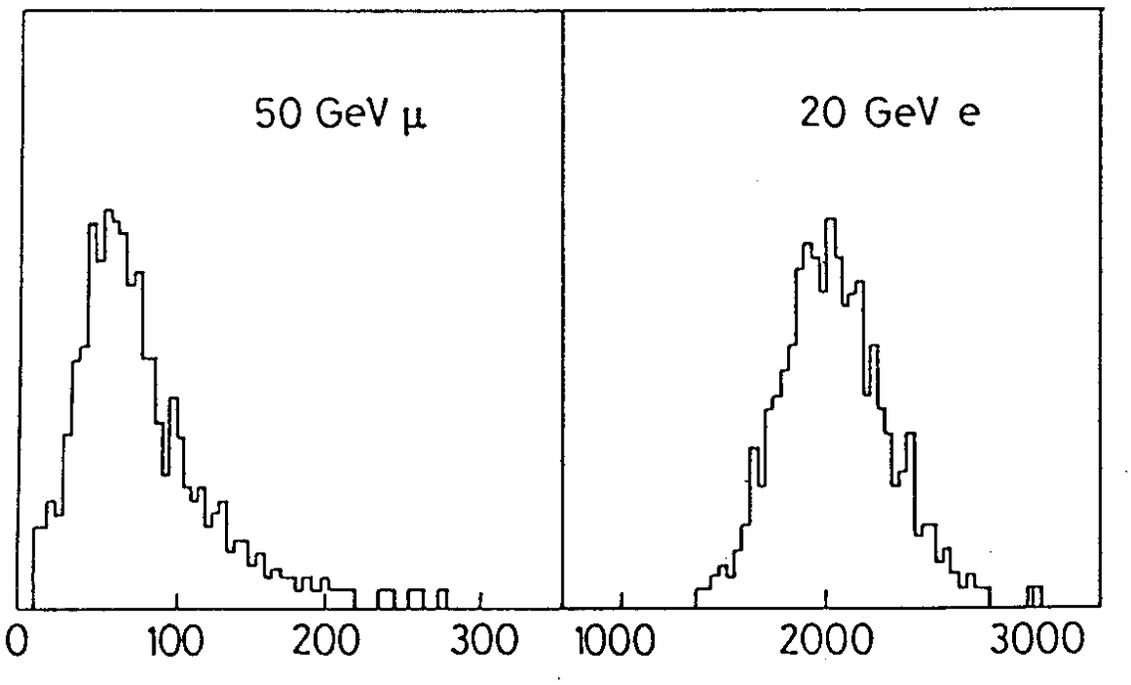

PULSE HEIGHT SPECTRA

FIG 15

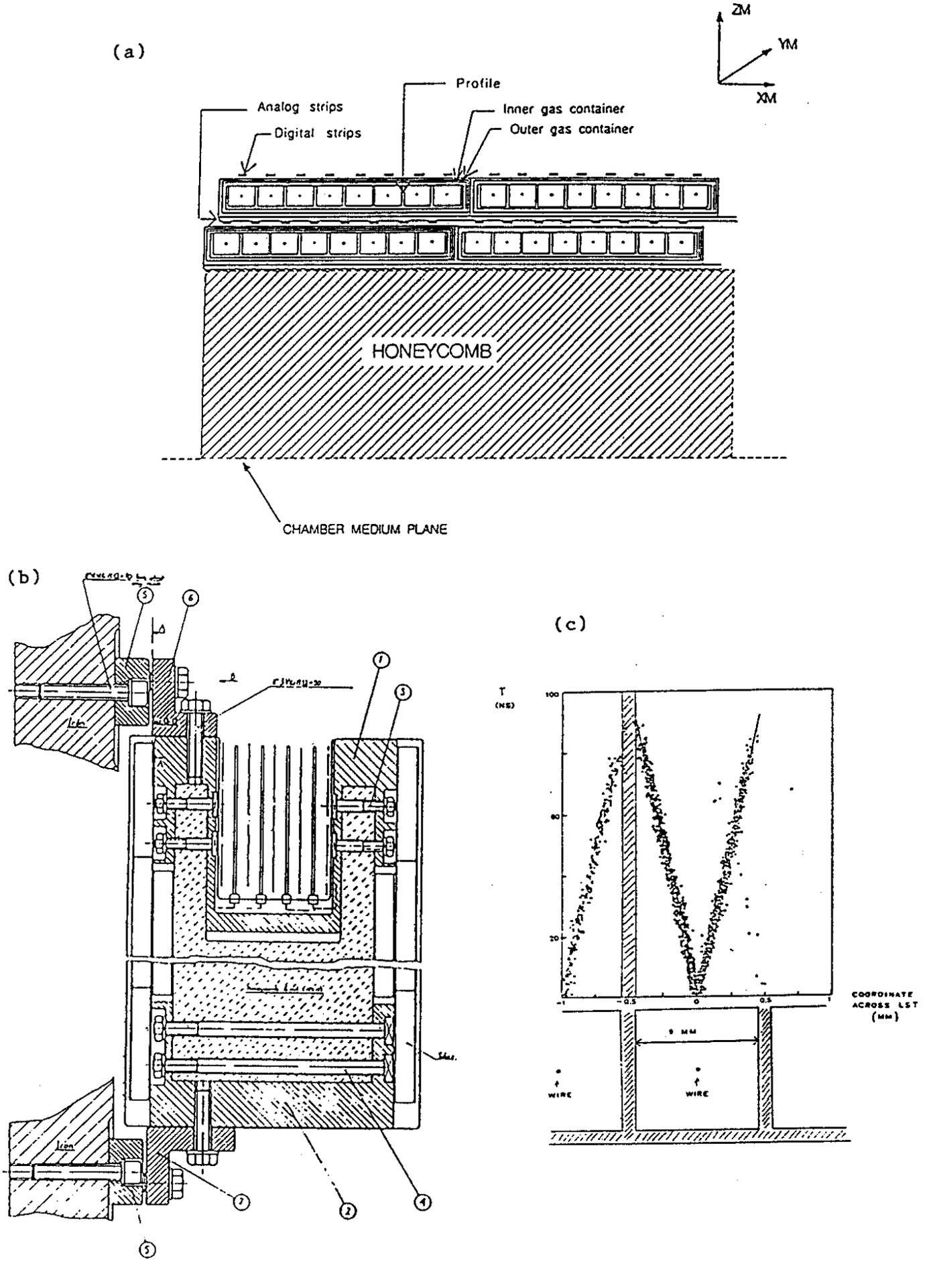
(a)
ZM
YM
XM
Profile
Analog strips
Digital strips
Inner gas container
Outer gas container
HONEYCOMB
CHAMBER MEDIUM PLANE
(b)
(c)
T
(NS)
100
80
20
-1
-0.5
0
0.5
1
COORDINATE
ACROSS LST
(MM)
8 MM
WIRE
WIRE

FIG 16

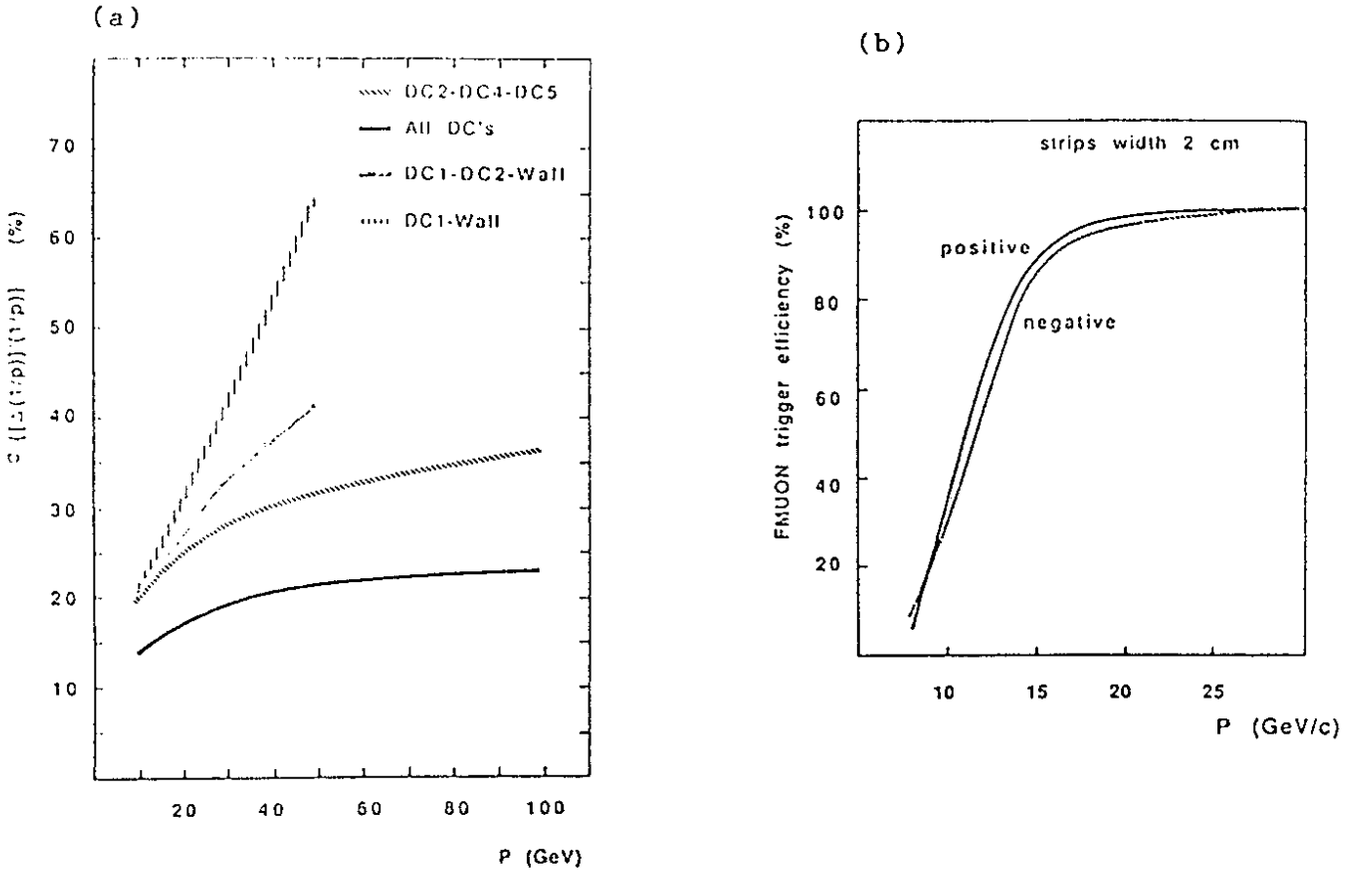
(a)
DC2-DC4-DC5
All DC's
DC1-DC2-Wall
DC1-Wall
70
60
50
40
30
20
10
20
40
60
80
100
P (GeV)
(b)
strips width 2 cm
positive
negative
FMUON trigger efficiency (%)
100
80
60
40
20
10
15
20
25
P (GeV/c)

FIG 17

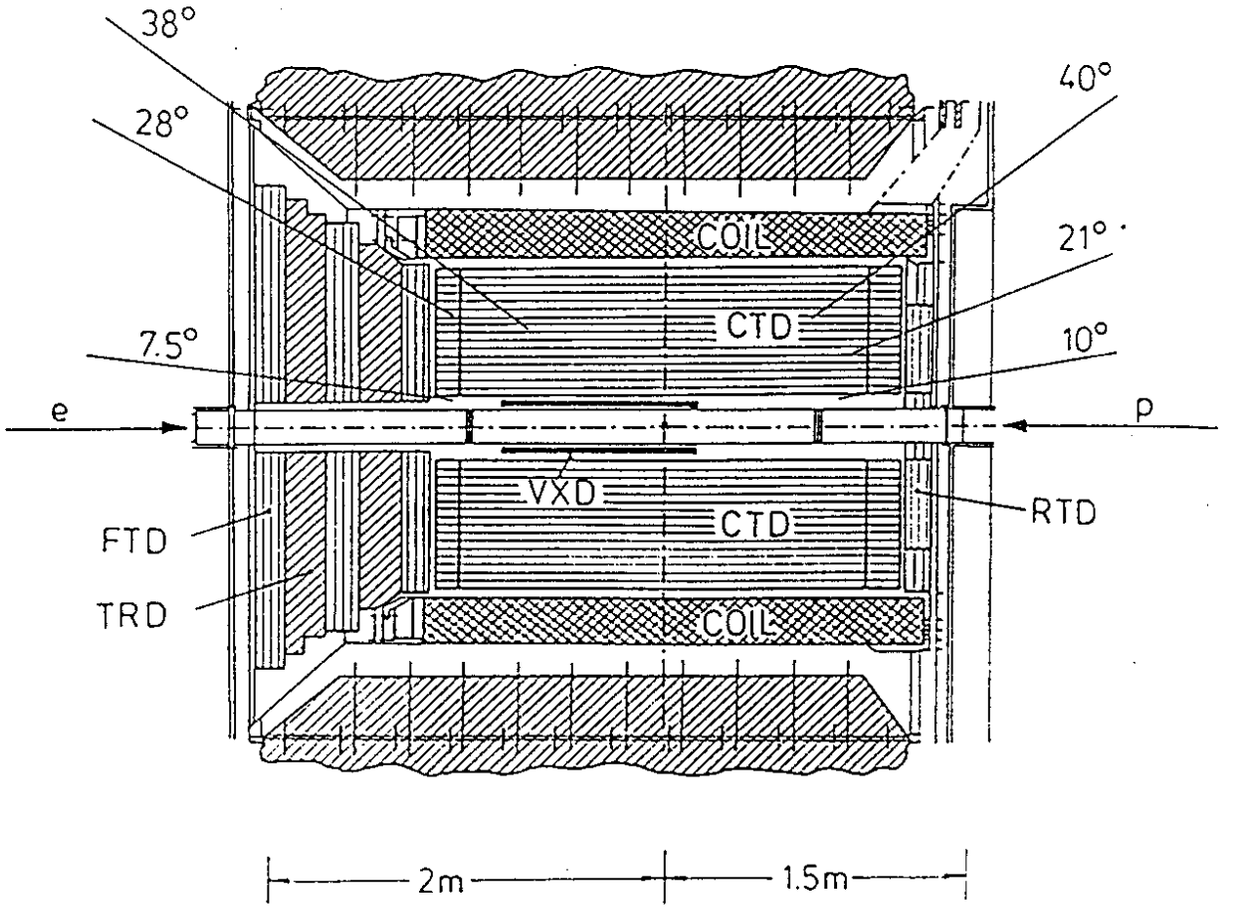
38°
28°
40°
21°
10°
7.5°
COIL
CTD
e
p
VXD
CTD
RTD
FTD
TRD
COIL
2m
1.5m

FIG 18

(a)

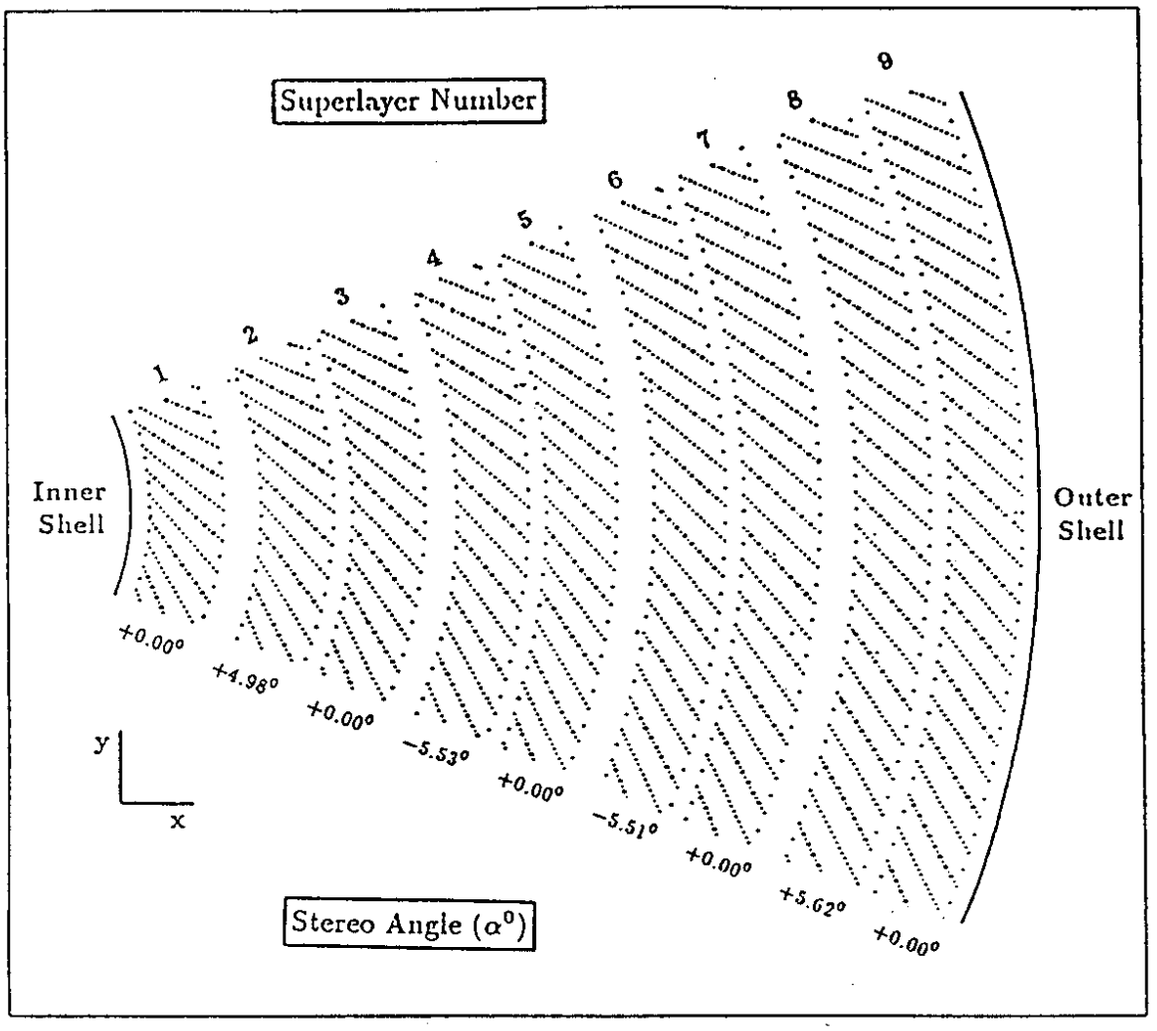
Superlayer Number
1
2
3
4
5
6
7
8
9
Inner Shell
Outer Shell
+0.00°
+4.98°
+0.00°
−5.53°
+0.00°
−5.51°
+0.00°
+5.62°
+0.00°
y
x
Stereo Angle (α°)

(b)

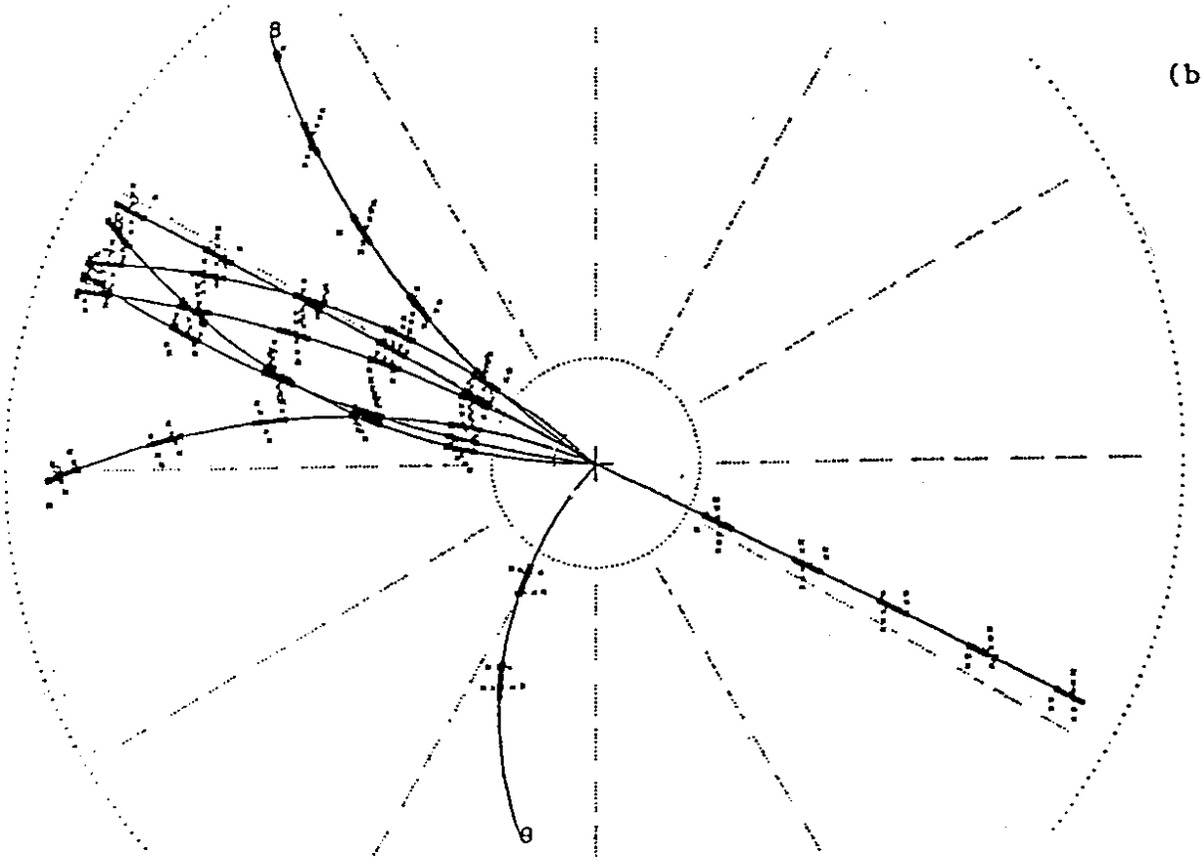
8
9

FIG 19

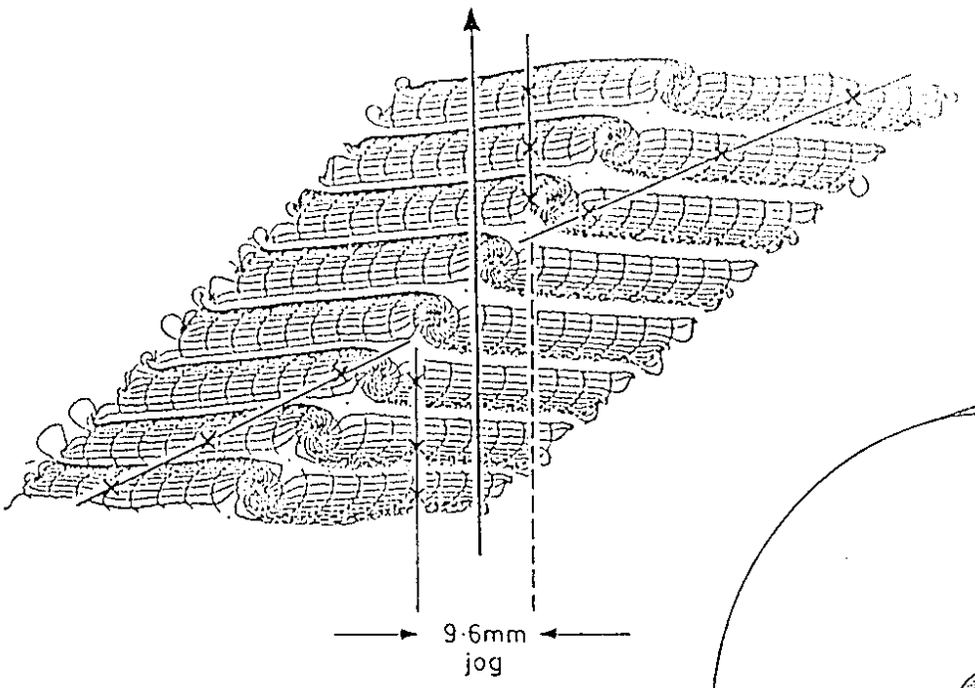

FIG 20

(a)

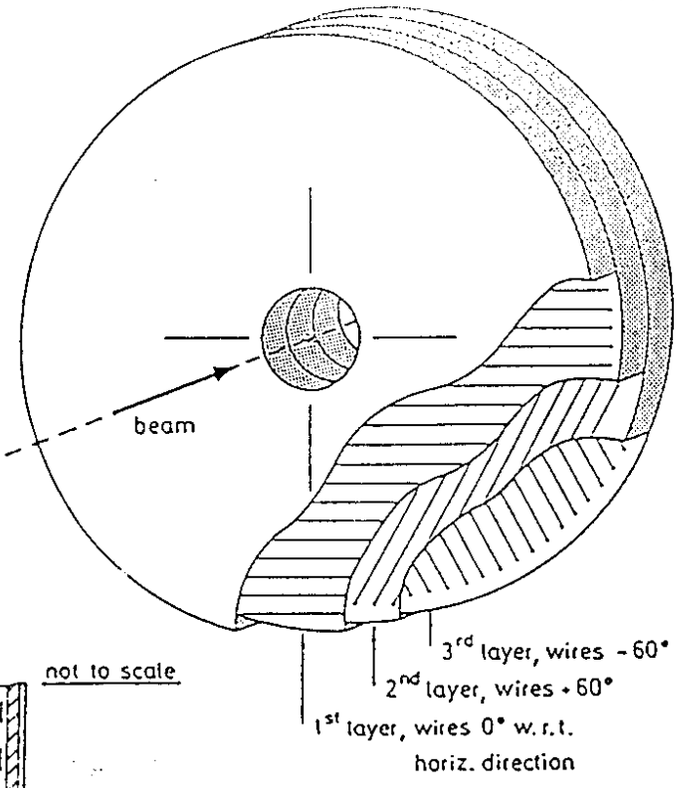

(b)

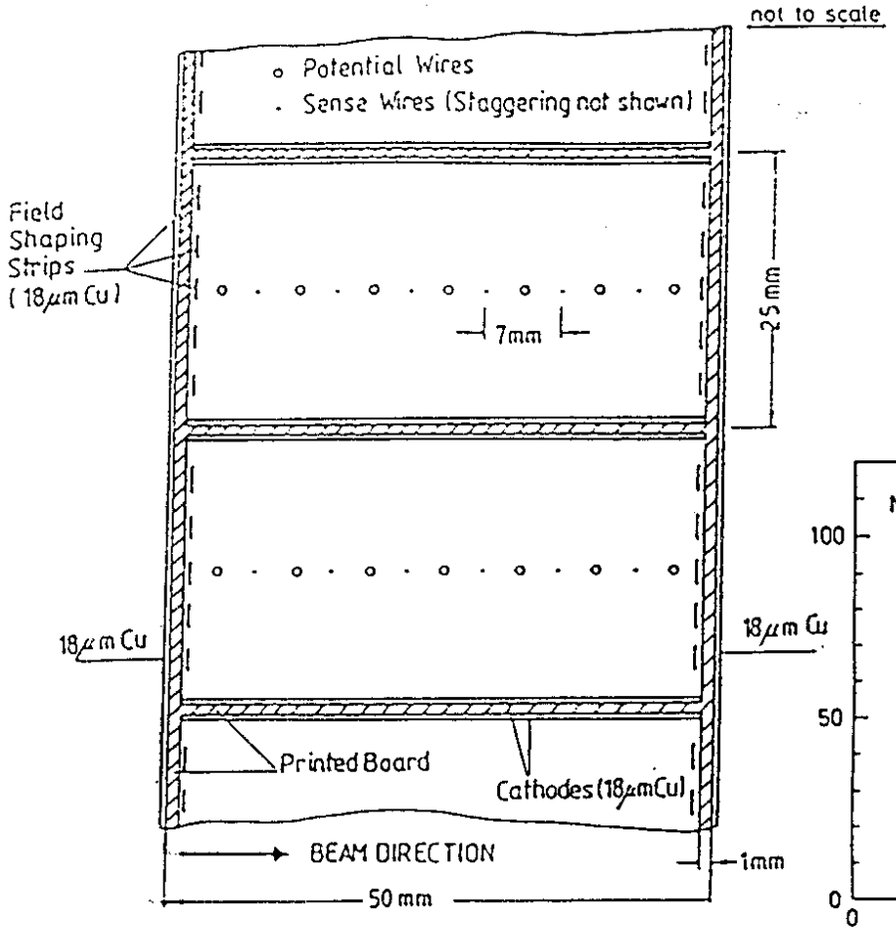

FIG 21

(c)

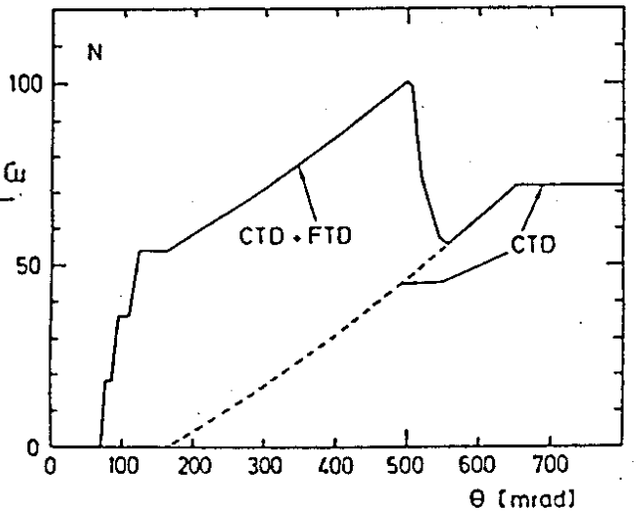

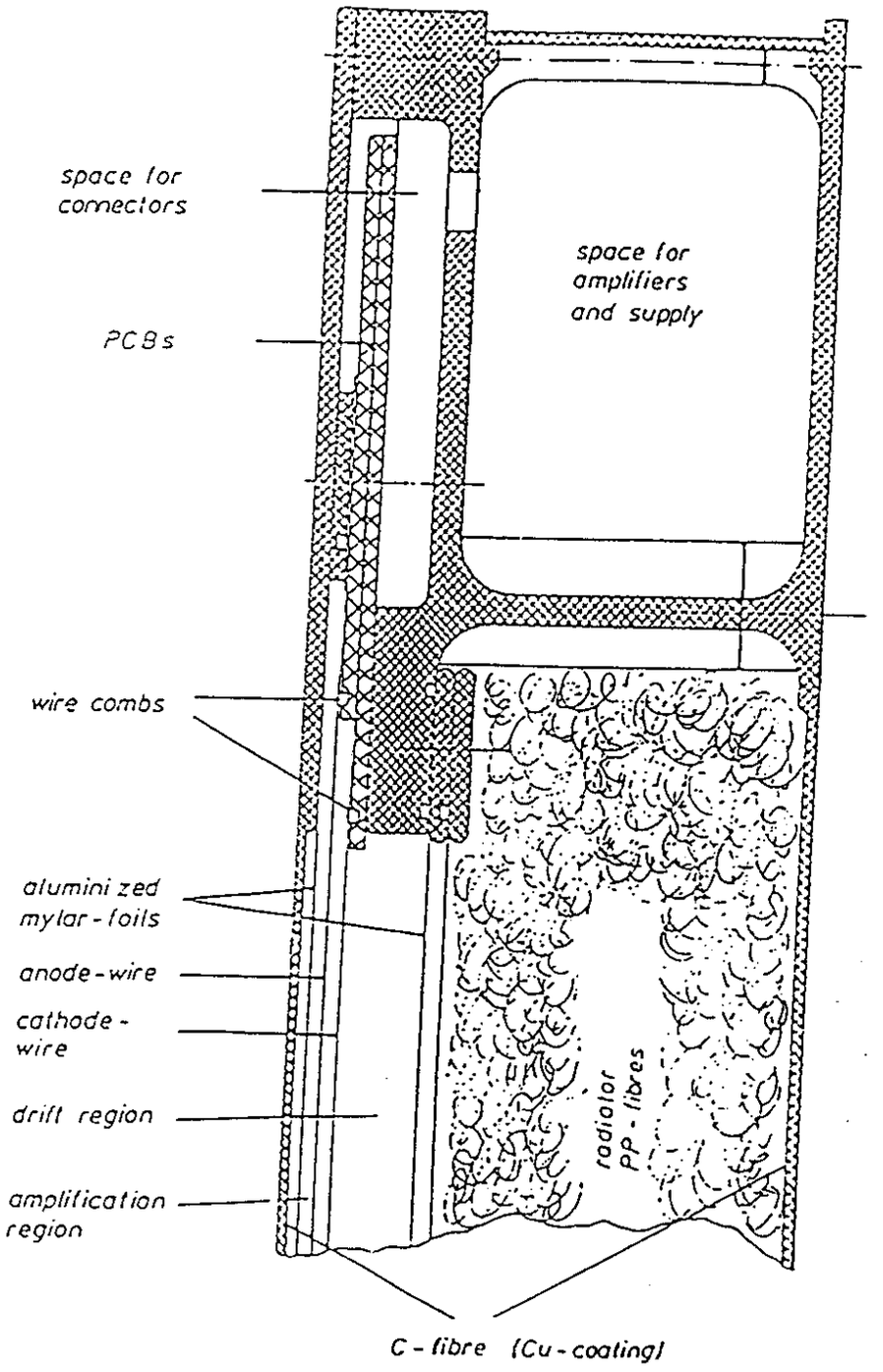

scale 1:1

50

FIG 22

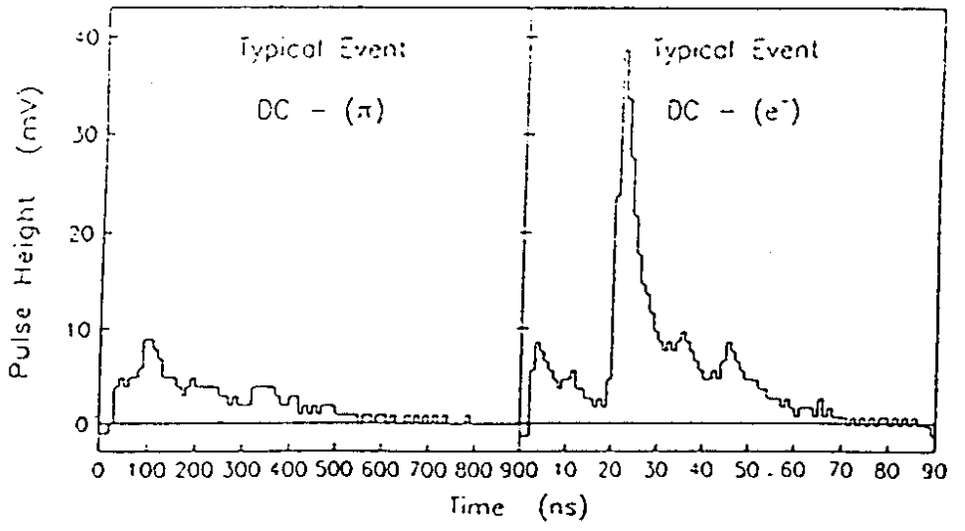

FIG 23

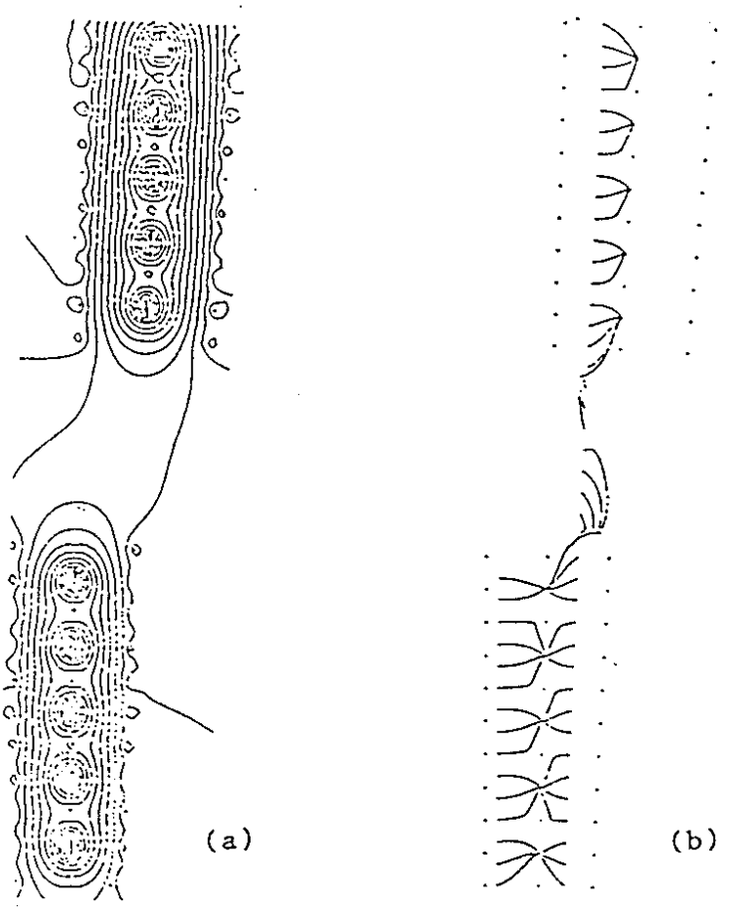
(a)
(b)

FIG 24

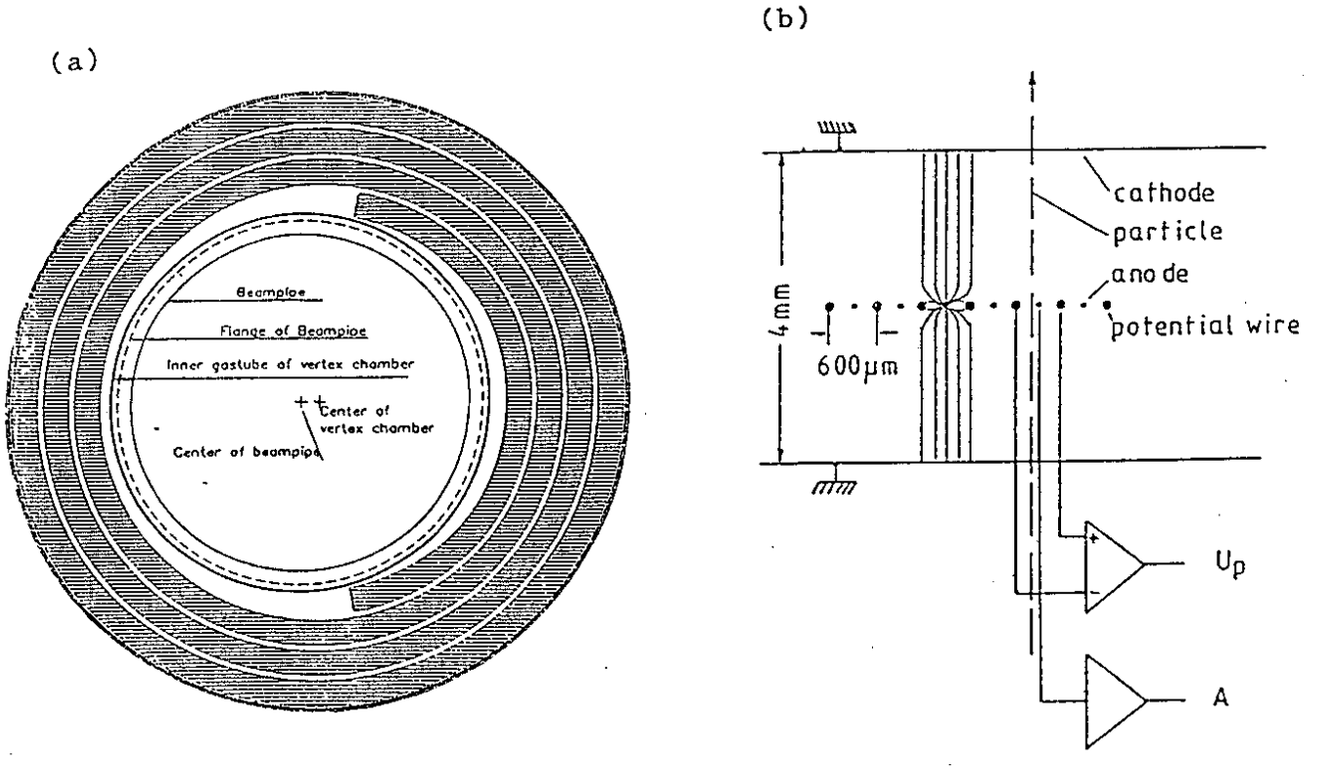
(a)
Beampipe
Flange of Beampipe
Inner gastube of vertex chamber
Center of vertex chamber
Center of beampipe
(b)
cathode
particle
anode
potential wire
4mm
600µm
Up
A

FIG 25

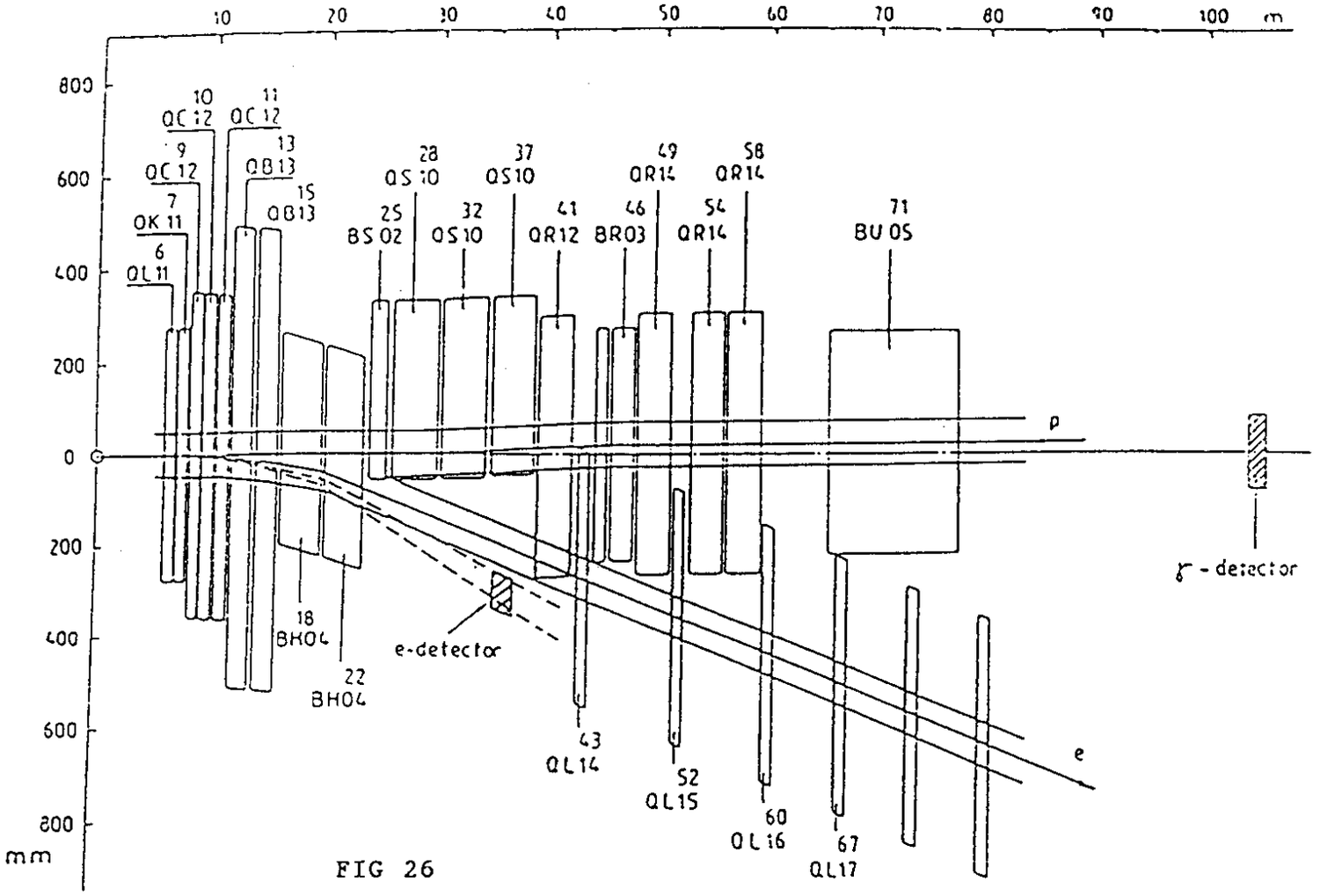

FIG 26

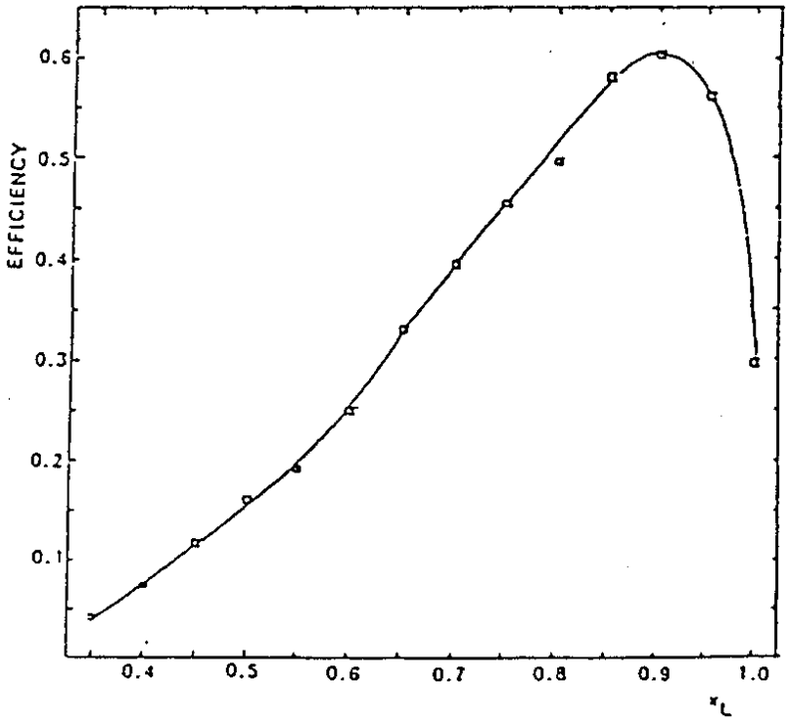

FIG 27(b)

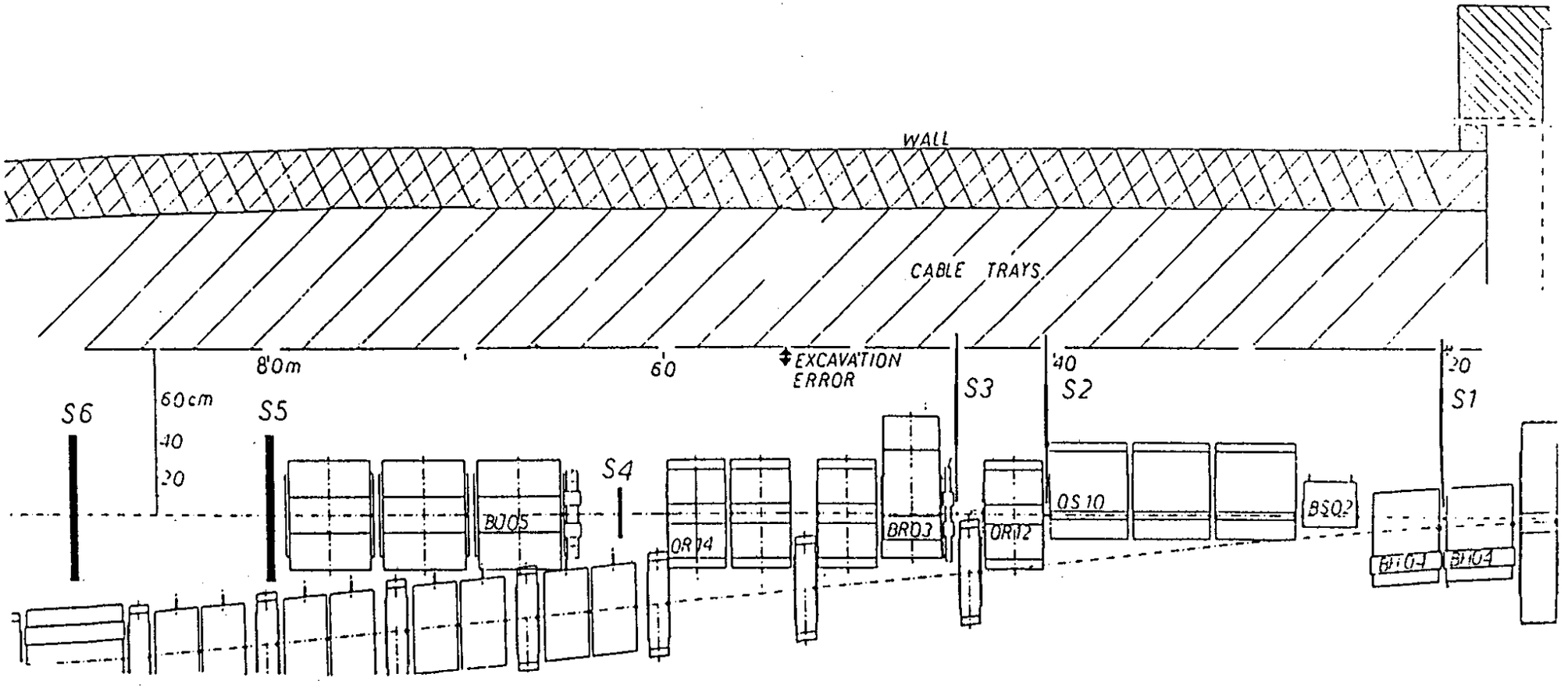
WALL
CABLE TRAYS
8'0m
60
EXCAVATION ERROR
40
20
60 cm
40
20
S6
S5
S4
S3
S2
S1
BQ05
OR04
BR03
OR02
OS 10
BSQ2
BR04

FIG 27(a)